OFF-AXIS NEUTRON STUDY FROM A UNIFORM SCANNING PROTON BEAM USING MONTE CARLO CODE FLUKA

By

MOHAMMAD RAFIQUL ISLAM

Bachelor of Science
University of Dhaka
Dhaka, Bangladesh
2003

Submitted to the Faculty of the
Graduate College of the
Oklahoma State University
in partial fulfillment of
the requirement for
the Degree of
MASTER OF SCIENCE
May, 2013

OFF-AXIS NEUTRON STUDY FROM A UNIFORM SCANNING PROTON BEAM USING MONTE CARLO CODE FLUKA

Thesis Approved:

Eric Benton

_____

Thesis Advisor

Eduardo G Yukihara

_____

Committee Member

Jerimy C Polf

_____

Committee Member

ACKNOWLEDGEMENT

I would like to thank my advisor, Dr. Eric Benton for his guidance, encouragement, and incessant support throughput this project. A time to time discussion with him on this project made me confident, focused and more motivated. I would also like to thank Dr. Art Lucas, Joel Dewitt, Carl Johnson, Tyler Collums, Jonathon Monson, Aaron Ruse, Nathan Lindy, and Robert Honeyman, for their help and support.

I would like to thank my wife, Maliha Rahman and my son Nameer, for their love, support, and presence during the challenging period of this project.

My sincere thanks to my parents for their support for my whole life and without them I could never come this far. My parents always had confidence in me that I can do better and that inspiration helped and encouraged me in successfully completing this work.

I would also like to thank Dr. Yuanshui Zheng for his generous support, especially for the information about the beam delivery system used at ProCure Proton Therapy Center, Oklahoma City, OK. I would also like to thank my Committee members, Dr. Eduardo Yukihara, and Dr. Jerimy Polf, for their support in this project.

Special thanks to FLUKA authors and the FLUKA discussion forum for their help, especially Vasilis Vlachoudis for his help on the successful simulation of this project.

Name: MOHAMMAD RAFIQUL ISLAM

Date of Degree: May, 2013

Title of Study: OFF-AXIS NEUTRON STUDY FROM A UNIFORM SCANNING PROTON BEAM USING MONTE CARLO CODE FLUKA

Major Field: Physics

ABSTRACT:

The production of secondary neutrons is an undesirable byproduct of proton therapy. It is important to quantify the contribution from secondary neutrons to patient dose received outside the treatment volume. The purpose of this study is to investigate the off-axis dose equivalent from secondary neutrons using the Monte Carlo radiation transport code FLUKA. The study is done using a simplified version of the beam delivery system used at ProCure Proton Therapy Center, Oklahoma City, OK. In this study, a particular set of treatment parameters were set to study the dose equivalent outside the treatment volume inside a phantom and in air at various depths and angles with respect to the primary beam axis. Three different proton beams with maximum energies of 78 MeV, 162 MeV and 226 MeV and 4 cm modulation width, a 5 cm diameter brass aperture, and a small snout located 38 cm from isocenter were used for the study. The FLUKA calculated secondary neutron dose equivalent to absorbed proton dose, H_n/D_p, decreased with distance from beam isocenter. The H_n/D_p ranged from 0.11 ± 0.01 mSv/Gy for a 78 MeV proton beam to 111.01 ± 1.99 mSv/Gy for a 226 MeV proton beam. Overall, H_n/D_p was observed to be higher in air than in the phantom, indicating the predominance of external neutrons produced in the nozzle rather than inside the body.

TABLE OF CONTENTS

Chapter Page

1 INTRODUCTION 1

2 PROTON RADIOTHERAPY 6
2.1 General Radiotherapy 6
2.1.1 Types of Radiotherapy 10
2.2 Rationale for using Proton Radiotherapy 12
2.3 Basics of Proton Therapy 15
2.4 Spread out Bragg peak 19
2.5 Beam Delivery Techniques 22
2.5.1 Passive Scattering 22
2.5.2 Active Scanning Technique 25
2.6 Secondary Neutron Production 29
2.7 Secondary neutron interaction with matter 33
2.8 Total cross section of secondary neutrons on tissue 34

3 DOSIMETRIC QUANTITIES 39
3.1 Particle Fluence 39
3.2 Linear Energy Transfer (LET) 40
3.3 Absorbed dose and dose equivalent 41
3.4 Guidelines to leakage Radiation Exposure 45

4 FLUKA SIMULATIONS 47
4.1 Monte Carlo Code FLUKA 47
4.2 Simulation of simplified snout 52
4.3 Simulation setup 54
4.4 Beam Interaction with snout and Phantom 57
4.5 SOBP Calculation 59

5 RESULTS 63
5.1 Neutron dose equivalent inside the phantom and in air 63
5.2 Neutron dose equivalent dependence on energy 76
5.3 Dependence of dose equivalent on angle 78

6 DISCUSSION AND CONCLUSIONS 80

7 REFERENCES 84

LIST OF TABLES

Table Page

Table 2.1: Energy taken up by various particles as a result of 150 MeV protons incident on ^{16}O nucleus (Seltzer, 1993). 17
Table 2.2: Atomic percentages for ICRU muscle (Collums, 2012) and water. 38
Table 3.1: Radiation weighting factor, w_R, as defined in ICRP-60 (ICRP, 1991) for neutron of different energy range. 43
Table 5.1: FLUKA simulated ratios of neutron dose equivalent to proton absorbed dose (H_n/D_p) for a 78 MeV primary proton beam at detector locations inside the phantom and in air. All the distance is measured from beam isocenter. 64
Table 5.2: FLUKA simulated ratios of neutron dose equivalent to proton absorbed dose (H_n/D_p) for a 162 MeV primary proton beam at detector locations inside the phantom and in air. All the distance is measured from beam isocenter. 70
Table 5.3: FLUKA simulated ratios of neutron dose equivalent to proton absorbed dose (H_n/D_p) for a 226 MeV primary proton beam at detector locations inside the phantom and in air. All the distance is measured from beam isocenter. 73
Table 6.1: Comparison of this study with other published work. The H_n/D_p value ... 82

LIST OF FIGURES

Figure Page

Figure 2.1: A double helical DNA molecule. The four bases are Guanine, Thymine, Cytosine, Adenine. Picture was taken from (DNA, 2013). 8
Figure 2.2: A schematic representation of direct and indirect action. Picture was adapted from (Hall and Giaccia, 2006). 9
Figure 2.3: Range of proton beam in water. Data taken from NIST website (NIST, 2012). 12
Figure 2.4: Comparison of depth dose curve for x-rays (20MV), electrons (4MeV), and protons (150 MeV) beams. Picture taken from (Wikimedia, 2013).... 14
Figure 2.5: A comparison of dose distribution in a patient due to photon and proton beam for medulloblastoma (Terezakis et al., 2011). 15
Figure 2.6: A Bragg peak for 200 MeV proton beam in water (Jones and Schreuder, 2001) 19
Figure 2.7: A common range modulator wheel used in proton radiotherapy. Picture taken from (Schlegel et al., 2006). 20
Figure 2.8: Illustration of the SOBP production using a range modulator for the maximum 200 MeV proton energy (ICRU, 2007) 21
Figure 2.9: Schematic diagram of passive scattering system for proton radiotherapy. 23
Figure 2.10: A custom patient aperture (left), and a custom made range compensator (right). Picture taken from (Decimal, 2013) 25
Figure 2.11: Schematic diagram of spot scanning delivery system in proton radiotherapy. 27
Figure 2.12: Schematic diagram of IBA uniform scanning nozzle. The components in the nozzle is not in scale 29
Figure 2.13: Illustration of intranuclear cascade and evaporation process. 32
Figure 2.14: Different types of neutron interaction. 33
Figure 2.15: A schematic representation of neutron interaction with carbon (top), and oxygen (bottom) nucleus, results three and four alpha particles respectively. Picture taken from (Hall and Giaccia, 2006). 35
Figure 2.16: A schematic representation of fast neutron's interaction with hydrogen atom inside tissue (Hall and Giaccia, 2006). 36
Figure 2.17: The average total cross section of neutron for carbon, oxygen and hydrogen as a function of incident neutron energy (NNDC). 37
Figure 2.18: The average total cross section of neutron for ICRU muscle and water as a function of incident neutron energy(NNDC, 2013). ICRU muscle cross section is multiplied by 10 in the graph for clarity 38

Figure 3.1: Quality factor, Q, as a function of LET as defined in ICRP Publication No. 60 (ICRP, 1991). 42
Figure 3.2: Ambient dose equivalent coefficients as a function of neutron energy. Plot taken from (Roesler and Stevenson, 2006). 45
Figure 4.1: Illustration of Monte Carlo approach using an isotropic neutron source. Picture taken from (Hendricks, 1994) 48
Figure 4.2: The cross sectional diagram of the snout (top), FLUKA geometry generated diagram of the snout (bottom). The snout is used at ProCure Proton Treatment Center, Oklahoma City, OK (Figure is not in scale). 53
Figure 4.3: Diagram of the setup with the presence of phantom. Dotted circles represent the detectors locations where dose equivalent was calculated inside the phantom. 55
Figure 4.4: Diagram of the experimental setup in air. Circles represent the detectors locations. 56
Figure 4.5: FLUKA simulated 3D view of a 162 MeV proton beam interacting with the snout and phantom 58
Figure 4.6: FLUKA simulated 2D view of 162 MeV primary beam interaction with snout and the phantom 59
Figure 4.7: Bragg-peak of individual primary proton beam and the calculated SOBP for the maximum energy of 226 MeV. 61
Figure 4.8: The generated SOBP for 78 MeV, 126 MeV and 226 MeV proton beam. . 62
Figure 5.1: FLUKA simulated neutron dose equivalent per therapeutic proton absorbed dose, H_n/D_p, for a 78 MeV proton beam inside the phantom at increasing distances from isocenter at 45°, 90° and 135° to the direction of the beam. 65
Figure 5.2: FLUKA simulated neutron spectrum from a 78 MeV proton beam inside phantom at 90° and 7.5 cm, 17.5 cm, 28.5 cm, and 35.5 cm from isocenter 66
Figure 5.3: FLUKA simulated neutron dose equivalent per therapeutic proton absorbed dose, H_n/D_p, for a 78 MeV proton beam in air at increasing distances from isocenter at 45°, 90° and 135° to the direction of the beam. 67
Figure 5.4: FLUKA simulated neutron dose equivalent per therapeutic proton absorbed dose, H_n/D_p, for a 78 MeV proton beams inside phantom and air at increasing distances from isocenter at 45°, 90° and 135° to the direction of the beam. 68
Figure 5.5. FLUKA simulated neutron spectrum for neutron energy of 1 to 20 MeV from a 78 MeV proton beam in air at 135° and 9.3 cm, 17.2 cm, 29.5 cm, and 33 cm from isocenter. 69

Figure 5.6: FLUKA simulated neutron dose equivalent per therapeutic proton absorbed dose, H_n/D_p, for a 162 MeV proton beam inside a phantom at increasing distances from isocenter at 45°, 90° and 135° to the direction of the beam. 71
Figure 5.7: FLUKA simulated neutron dose equivalent per therapeutic proton absorbed dose, H_n/D_p, for a 162 MeV proton beam in air at increasing distances from isocenter at 45°, 90° and 135° to the direction of the beam. 71
Figure 5.8: FLUKA simulated neutron dose equivalent per therapeutic proton absorbed dose, H_n/D_p, for a 162 MeV proton beams inside phantom and in air at increasing distances from isocenter at 45°, 90° and 135° to the direction of the beam. 72
Figure 5.9: FLUKA simulated neutron dose equivalent per therapeutic proton absorbed dose, H_n/D_p, for a 226 MeV proton beam inside a phantom at increasing distances from isocenter at 45°, 90° and 135° to the direction of the beam. 74
Figure 5.10: FLUKA simulated neutron dose equivalent per therapeutic proton absorbed dose, H_n/D_p, for a 226 MeV proton beam in air at increasing distances from isocenter at 45°, 90° and 135° to the direction of the beam. 75
Figure 5.11: FLUKA simulated neutron dose equivalent per therapeutic proton absorbed dose, H_n/D_p, for a 226 MeV proton beam inside a phantom and in air at increasing distances from isocenter at 45°, 90° and 135° to the direction of the beam. 75
Figure 5.12: Diagram of the locations where dose equivalent was calculated at 17.5 cm from isocenter inside the phantom (top) and in air (bottom). 76
Figure 5.13: FLUKA simulated neutron dose equivalent per therapeutic proton absorbed dose, H_n/D_p, at 17.5 cm, 90° to primary beam, for 78 MeV, 162 MeV and 226 MeV protons inside a phantom (left) and in air (right). 77
Figure 5.14: FLUKA simulated neutron dose equivalent per therapeutic proton absorbed dose, H_n/D_p, at 17.5 cm for 78 MeV, 162 MeV, 226 MeV protons inside the phantom (left), and in air (right). 79

CHAPTER 1

INTRODUCTION

The objective of radiation therapy is to deliver a high dose of ionizing radiation to the treatment volume (cancerous tumor), while simultaneously minimizing the radiation dose to the surrounding healthy tissue. In radiation therapy, the use of a proton beam as ionizing radiation has been considering promising in the last decade primarily because energetic protons have a finite range and can be used to deliver maximum dose to the treatment volume. However, the advantage of proton radiotherapy can be compromised due to the effects of secondary neutrons. Secondary neutrons are an undesired byproduct of proton radiotherapy and the exposure of secondary neutrons outside the treatment volume can lead to secondary cancer later in the patient's life. The aim of this work is to quantify the out of field dose equivalent due to secondary neutrons from uniform scanning beam delivery systems used in proton radiotherapy by means of simulations carried out using the Monte Carlo radiation transport code FLUKA.

In proton radiotherapy, secondary neutrons are produced when the primary proton beam is guided and shaped via passage through different materials inside the beam delivery system to conform the shape of the beam to the tumor (Zheng et al., 2007b, Mesoloras et al., 2006). Secondary neutrons are created mainly through non-elastic interactions of the primary protons of the treatment beam with atomic nuclei of the beam shaping materials (Perez-Andujar et al., 2009, Polf et al., 2005, Polf and Newhauser, 2005, Hecksel et al., 2010, Jiang et al., 2005, Zheng et al., 2007b, Zheng et al., 2008, Zheng et al., 2007a, Moyers et al., 2008, Binns and Hough, 1997). These secondary neutrons possess a wide range of energy, and sufficient range to reach deep into the patient's body. Since neutrons have higher relative biological effectiveness (RBE) compared to protons or x-rays (Paganetti, 2007, Hall, 2006), they are capable of doing more biological damage to tissue.

Exposure to secondary neutrons can increase the risk of secondary cancer later in a patient's life. Although the risk associated with exposure to secondary neutrons is not completely understood, a recent study showed that the associated risk for a 15 year male and female of developing a secondary cancer from secondary neutron exposure is about 20% and 44%, respectively (Brenner and Hall, 2008). Moreover, an understanding of the secondary radiation produced in proton radiotherapy is important for the optimization of dose delivery systems, shielding design, and overall quality of treatment.

The level of the secondary neutrons produced in proton radiotherapy depends on the design of the beam delivery system (Brenner et al., 2009, Tayama et al., 2006, Zheng et al., 2007a). Generally, there are two types of beam delivery system in proton radiotherapy: passive scattering and active scanning beam delivery systems. A detailed description of beam delivery system used in proton radiotherapy is given in section 2.5. Currently, both passive scattering and active scanning beam delivery systems are in use at different proton therapy centers, although passive scattering systems are used in the majority of facilities currently in operation (Koehler et al., 1977, Arjomandy et al., 2009). In the passive scattering beam delivery system, the primary proton beam energy (and hence range) is varied by a range modulator (usually low-Z) and a second scatterer foil (usually of high-Z) is used to laterally spread the beam on to the target (Perez-Andujar et al., 2009). Active beam delivery systems, on the other hand, are of two categories: pencil beam scanning and uniform beam scanning systems. In pencil beam scanning systems, dose is deposited to the target volume with the help of variable proton energy and intensity, and the system may not require any beam shaping components. In uniform scanning systems, the system uses beam shaping components like a range modulator, patient aperture, and range compensator similar to that used in passive systems except that it uses magnets instead of scattering foils to spread the beam over the treatment volume. Overall, the uniform scanning system uses less material in the beam path than a passive scattering delivery system and thereby presumably produces fewer neutrons (Arjomandy et al., 2009).

The uniform scanning beam delivery system in proton radiotherapy is a very recent development and few treatment centers currently use the uniform scanning method for patient treatment. The studies of secondary neutron dose due to uniform scanning are, therefore, scarce. The objective of this work was to quantify the dose equivalent due to secondary neutrons produced in the uniform scanning system inside the phantom patient and in air at different angles and locations relative to isocenter of the beam for different proton energies with a typical treatment set up. The study was carried out for the simplified version of the uniform beam delivery system used at ProCure Proton Therapy Center, Oklahoma City, OK.

This work describes radiation therapy and the rationale for proton radiotherapy in Chapter Two. The different types of beam delivery system that are currently used in proton radiotherapy are also discussed here. Chapter Three discusses the fundamental dosimetric quantities required for the calculation of absorbed dose and dose equivalent. The fluence to dose equivalent conversion factor is a major concern in numerical simulation and this is discussed in Chapter Three. The simulation of the study and relevant parameters like the neutron cross section library, particle threshold, etc. used in FLUKA are described in Chapter Four. Chapter Five presents the results of the FLUKA simulations for secondary neutrons in proton radiotherapy for uniform scanning system at different angles and location from beam isocenter inside the phantom and in air. The dose equivalent is presented as the ratio of secondary dose equivalent due to neutrons to primary proton dose, H_n/D_p. Finally,

Chapter Six compares results from this study with published data for similar passive scattering and uniform scanning beam delivery systems.

CHAPTER 2

PROTON RADIOTHERAPY

2.1 *General Radiotherapy*

The term radiation therapy or radiotherapy refers the use of ionizing radiation to kill or control tumor volume of cancer patients. The objective of radiotherapy is to deliver a high dose of ionizing radiation to a cancerous tumor in a noninvasive way, causing the cells of the tumor to die, while simultaneously minimizing the radiation dose to the healthy tissue surrounding the tumor.

Radiotherapy is considered as one of the most effective treatments for cancer and more than half of all cancer patients receive radiotherapy at some point in their treatment (Tobias, 1996, Delaney et al., 2005). Surgery, the preferred choice of treatment, is successful for tumors in an early stage i.e. when the cancer does not metastasize or spread to other organs. Radiotherapy is considered a good alternative to surgery for long term control of tumors in the lung, cervix, bladder, prostate, head and neck, skin, and other organs. Chemotherapy, the third most important form of treatment, uses chemical agents, i.e. drugs, to control the cancerous cells (Joiner and Kogel, 2009). But the diseases for which chemotherapy

alone is considered effective are rare. Studies suggest that radiotherapy along with surgery have a success rate of 40% for local treatments of most types of tumors (Souhami and Tobias, 1986, DeVita et al., 1979). Radiotherapy alone is suggested the principal form of treatment for about 15% of all types of cancers, whereas the cure rate due to chemotherapy is about 2% (Joiner and Kogel, 2009). Based on this study, it can be projected that the patient cure rate is around 7 times higher in radiotherapy compared to chemotherapy. However, depending on the stage of the cancer, radiotherapy is sometimes combined with chemotherapy or surgery for treating cancer patients. Generally, the precise treatment depends on the patient age, tumor location, stage of the tumor development and the general health of the patient.

When ionizing radiation strikes the tumor, the DNA of the cells can become damaged either through direct or indirect interaction. DNA molecules are double-stranded helices where the backbone is made of alternating sugar and phosphates; and the base pair consists of one of four nitrogen-containing biological compounds: guanine, thymine, cytosine, and adenine as shown in Figure 2.1 Cancer cells are generally less likely to repair the damage caused by direct or indirect action, compared to healthy cells, thus casing the cancer cells to reproduce more slowly or to die. An illustration of direct or indirect interaction is shown in Figure 2.2.

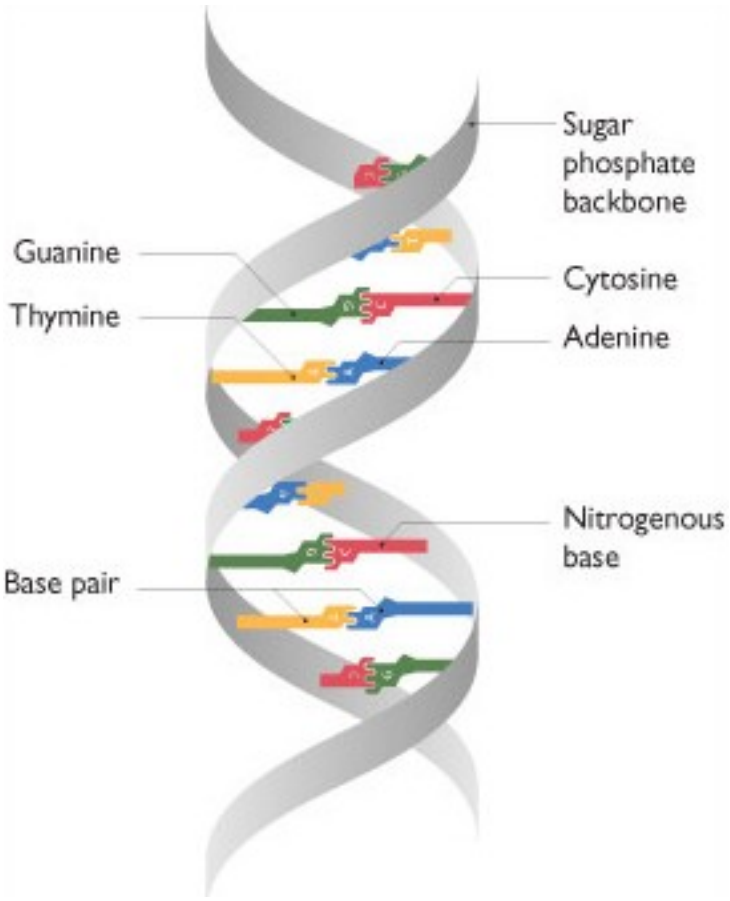

Figure 2.1: A double helical DNA molecule. The four bases are Guanine, Thymine, Cytosine, Adenine. Picture was taken from (DNA, 2013).

In direct interaction, ionizing radiation interacts directly with DNA of the cell. The damage to the cell occurs when ionizing radiation breaks one or both of the sugar phosphate backbones, the base pairs of the DNA, or some other cellular components essential for the survival of the cell.

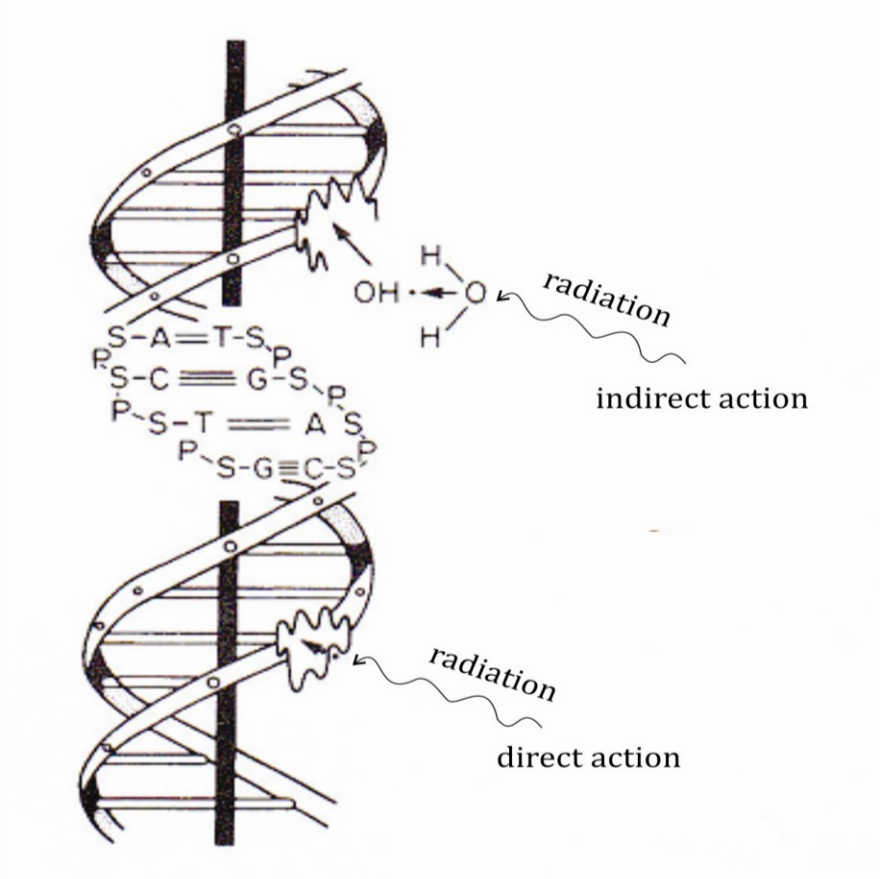

Figure 2.2: A schematic representation of direct and indirect action. Picture was adapted from (Hall and Giaccia, 2006).

Indirect reaction, on the other hand, occurs via free radical. A free radical is a molecule, atom or ion that has an unpaired orbital electron in the outer shell. When ionizing radiation interacts with a water molecule, (major constituent of the cell), it creates a free radical, H_2O^+ (positively charged molecule and has an unpaired electron in the outer shell). This reaction can be expressed as

$$radiation + H_2O \rightarrow H_2O^+ + e^-.$$

The ion radical interacts with another water molecule and forms a very reactive hydroxyl radical (OH^-), which can be shown as,

$$H_2O^+ + H_2O \rightarrow H_3O^+ + OH^-.$$

The hydroxyl free radicals (OH^-) are extremely reactive and cause harmful chemical reactions within the cell. It has been shown that about two thirds of all damage done to cells are due to hydroxyl free radicals in indirect interactions (Saha, 2006). Gamma and x-ray beam mostly damage the cell via indirect interactions, whereas energetic protons and carbons mostly damage the cell via direct interactions.

2.1.1 Types of Radiotherapy

Radiation therapy can be divided into two main groups: a) external beam radiation therapy (EBRT or XBRT), and b) internal radiotherapy. External beam radiation therapy uses an external source of radiation (outside the body) to treat cancerous tumors. X-rays and electrons are the most widely used form of radiation in external beam radiation therapy. Generally, low energy (kilovoltage) x-rays and electrons are used for superficial tumors and skin cancers. Megavoltage x-rays are usually used for deep seated tumors such as tumors in the prostate, lungs, etc. Apart from x-rays and electrons, protons and heavy ions are also used in external beam radiotherapy. External beam radiation therapy is further classified as conventional

and unconventional radiotherapy. Conventional radiotherapy includes x-ray and electron beam radiotherapy, while unconventional radiotherapy includes proton and heavy ion beam radiotherapy.

Internal radiation therapy, on the other hand, places radioisotope inside or on the body (Patel and Arthur, 2006) to deliver dose to the treatment volume. This can use both sealed and unsealed radioactive sources (NCI, 2013). Brachytherapy is the method that uses sealed radioactive sources positioned in and around the tumor. In this method, radioactive sources are placed either interstitialy (source placed inside the tumor), intracavity (source placed inside a cavity), or on the surface (source attached to the surface) (Khan, 2003). The most common types of radioactive sources used in brachytherapy are ^{125}I, ^{103}Pd, ^{192}Ir, ^{198}Au. In this type of radiation therapy, a significant dose can be delivered locally to the tumor while a rapid dose fall off occurs adjacent in the normal tissues. This is commonly used for treating cancers such as prostate, cervical, breast, skin, etc. The unsealed source of radiotherapy uses soluble forms of radioactive sources such as ^{131}I and is taken either via injection or ingestion. This is also called systematic radiotherapy (NCI, 2013). This form of radiation therapy is effective for only some types of thyroid cancer as thyroid cells naturally absorb both radioactive and stable iodine (NCI, 2013). However, depending on the tumor stage, a combination of external and internal beam therapy is sometimes prescribed.

2.2 *Rationale for using Proton Radiotherapy*

Among different types of radiotherapy, the use of x-rays or electrons is the most common (99% of all forms of radiotherapy) (Sisterson, 2005), while proton and heavy ion radiotherapy makes up less than 1%. However, in conventional radiotherapy, the dose distribution to surrounding healthy tissue is significantly higher due to the greater scattering of x-rays or electrons inside the tissue than in proton or heavy ion radiotherapy.

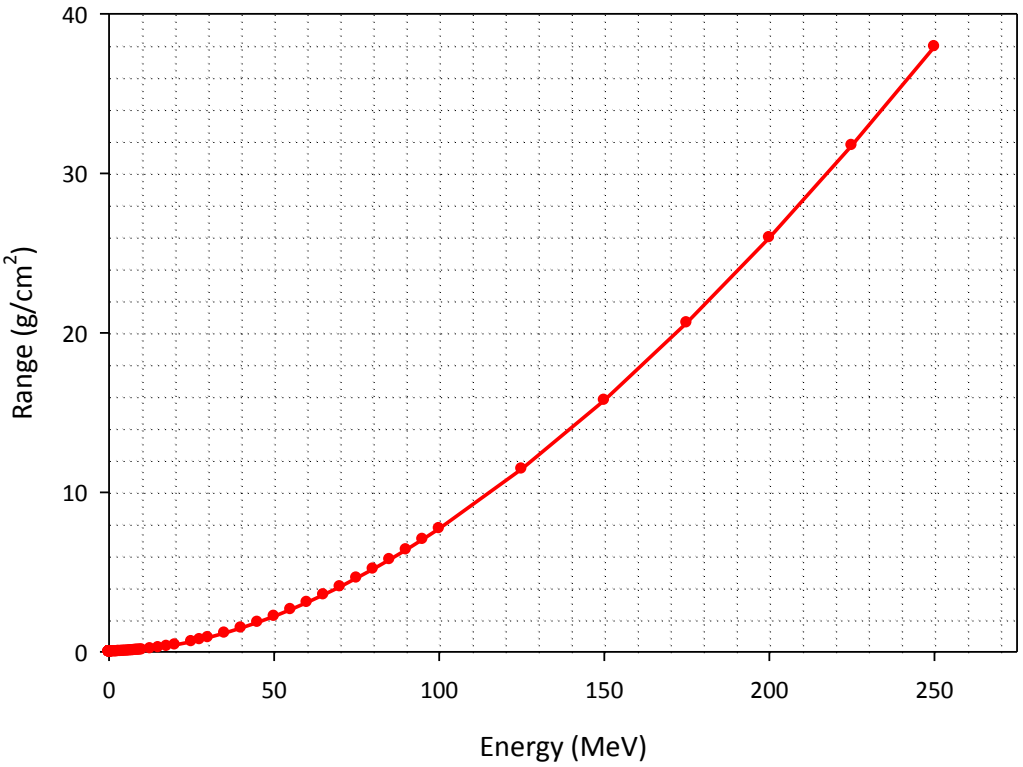

Figure 2.3: Range of proton beam in water. Data taken from NIST website (NIST, 2012).

This problem is better handled by proton beams since protons are relatively heavy and have finite range in matter. The range of proton beam of therapeutic energy in water is shown in Figure 2.3 (NIST). A proton of a given kinetic energy has a finite, known range in water or tissue. Also, proton delivers maximum of its energy at the end of its range. Due to this property, protons deliver most of its energy at a certain range and the relatively large mass of proton leads to less scatter as they travel through the tissue. On the other hand, x-rays do not possess a finite range; rather they attenuate exponentially with depth in tissue. Due to these inherent properties, protons can be used to deliver a higher dose to the tumor while minimizing dose adjacent to the healthy tissue. X-rays, unlike protons, deliver its maximum dose near the entrance and the exponential dose fall off with depth causes a considerably higher dose to the healthy tissue.

An example of dose deposition in tissue as a function of depth due to x-rays (20MV), electrons (4MeV), and protons (150 MeV) is shown in Figure 2.4. This figure shows that protons deliver most of their dose at the end of its range while the dose due to x-rays follows an exponential pattern. Electron beams show a greater dose fall off but clinically this advantage disappears as electrons do not possess great penetrating property. This leaves the use of electron beam radiotherapy effective mostly for shallow tumors.

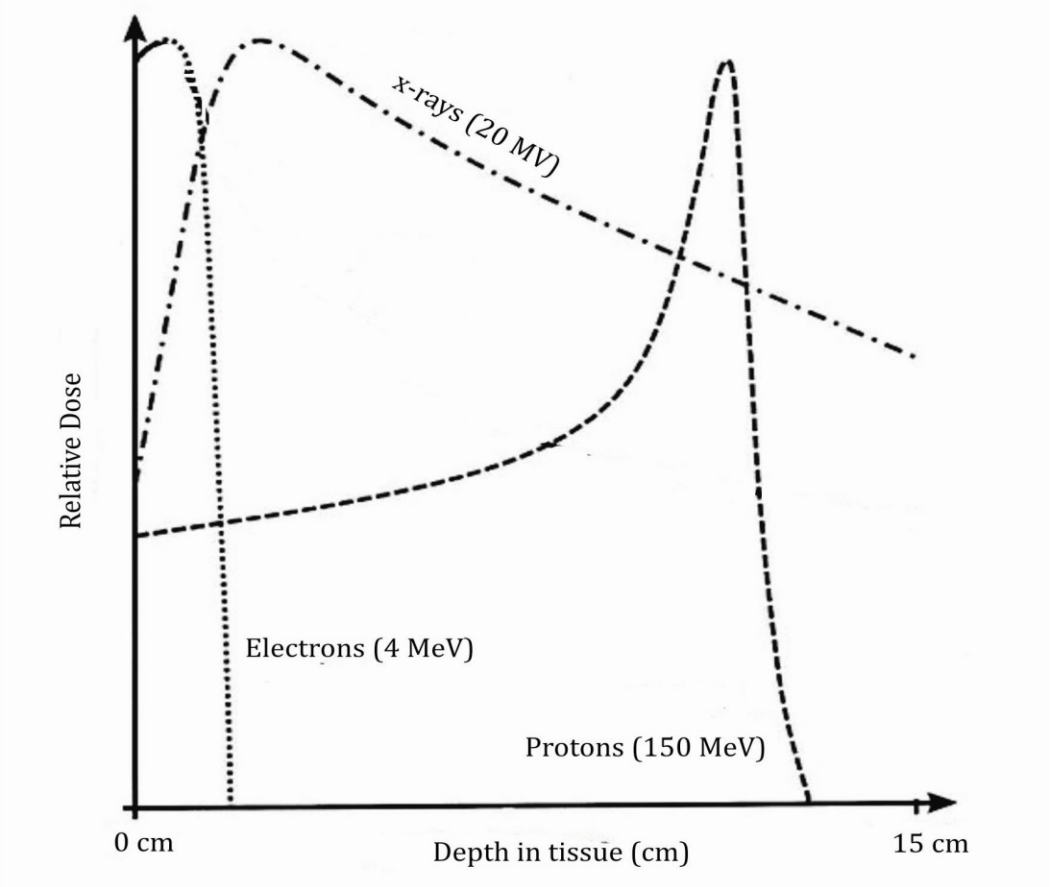

Figure 2.4: Comparison of depth dose curve for x-rays (20MV), electrons (4MeV), and protons (150 MeV) beams. Picture taken from (Wikimedia, 2013).

A clinical example of dose distribution by x-ray and proton radiotherapy in a patient for the disease medulloblastoma is shown in the Figure 2.5 (Terezakis et al., 2011). This figure shows that the dose distribution, (shown by the different shades of color) due to photon beam (top) is larger than that of proton beam (bottom). Clinically this advantage of precise dose distribution has led proton radiotherapy to be a superior modality compared to photon and electron radiotherapy (Dowdell, 2011). For this reason, proton radiotherapy has been proving effective in critical

cases such as tumors in head and neck (Steneker et al., 2006, Dowdell, 2011), ocular tumors (Dendale et al., 2006), and tumors in pediatric patients (Dowdell).

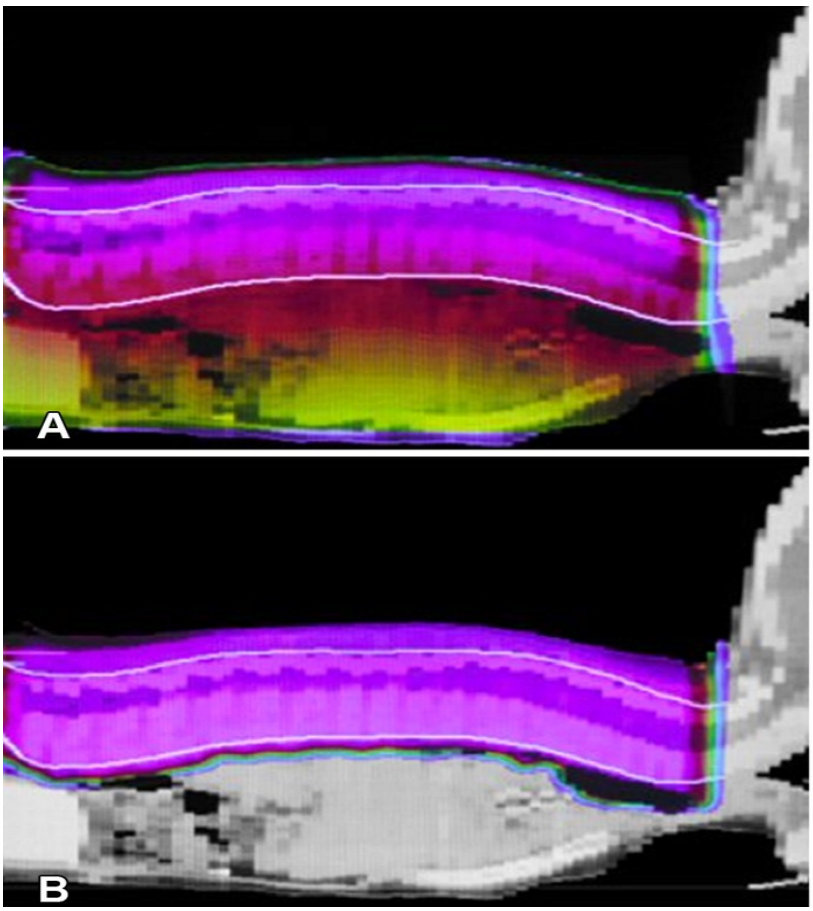

Figure 2.5: A comparison of dose distribution in a patient due to photon and proton beam for medulloblastoma (Terezakis et al., 2011).

2.3 *Basics of Proton Therapy*

The energetic protons of a proton radiotherapy beam interact with matter as they pass through it by three different mechanisms (Goitein, 2008): a) coulomb

interactions with atomic electrons, b) coulomb interactions with atomic nuclei, and c) nuclear interactions with atomic nuclei. Coulomb interactions with atomic electrons occur as the positively charged protons interact with negatively charged orbital electrons, transferring kinetic energy to the atomic electrons and producing ionization and excitation of the atoms. In ionization, the interacting protons transfer sufficient energy to knock out one or more electrons from the target atom. These secondary electrons can possess sufficient energy to cause further ionization in the region surrounding the initial interaction. Since protons are much heavier than electrons, the deflection of protons in this process is negligible. Protons also interact via coulomb fields of atomic nuclei as they penetrate through matter. Repulsion between incoming protons and atomic nuclei scatter protons, since nuclei are of equal or greater mass than the incident protons. However, after many such scattering events, the net statistical deflection is typically very small (Goitein, 2008). Nuclear interactions with atomic nuclei via the strong nuclear force is another process that leads to two types of collisions elastic collisions and non-elastic collisions. In elastic collisions, protons lose significant amounts of energy, but the target nucleus is left intact. In non-elastic collision, the incident protons penetrate the target nucleus and may cause the nucleus to break apart. As a result of non-elastic nuclear collisions, fragments of the target nucleus may escape the region with a large momentum and may possess considerable kinetic energy. An example of such an interaction is shown in Table 2.1 for a 150 MeV protons on ^{16}O (Seltzer, 1993).

Table 2.1: Energy taken up by various particles as a result of 150 MeV protons incident on ^{16}O nucleus (Seltzer, 1993).

Particle	Fraction of energy (%)
Protons	57
Neutrons	20
Alpha particles	2.9
Deuterons	1.6
Tritium	0.2
Helium-3	0.2
Recoil fragments	1.6

The primary mechanism for energy loss by protons passing through matter is due to Coulomb interactions with atomic electrons in the medium. The loss of energy due to Coulomb interactions can be calculated using the Bethe-Bloch formula (Bethe, 1930):

$$-\frac{dT}{dx} = \frac{n_e e^4}{4\pi\varepsilon_0^2 m v^2} L, \qquad 2.1$$

where $-\frac{dT}{dx}$ is the energy lost by the incident charged particle proton per unit path length, n_e represents the electron density of the target, e represents electron charge, ε_0 represents the permittivity of free space, m is the rest mass of the electron, L represents a collection of logarithmic factors and correction factors and is given by:

$$L = \ln\left(\frac{2mv^2}{I}\right) - \ln\left(1 - \frac{v^2}{c^2}\right) - \frac{v^2}{c^2} - \frac{\delta}{2}. \qquad 2.2$$

The standard relativistic corrections, $-\ln(1 - v^2/c^2) - v^2/c^2$, are important if the projectile in the interaction is moving at a significant fraction of the speed of light. If the velocity of the projectile is small compared to the speed of light, equation (2.2)

simplifies to $L \cong \ln(2mv^2/I)$, where v is the velocity of the incident charged particle and I is the mean ionization potential. The term, $\delta/2$, in equation (2.2) represents the density effect correction (Sternheimer and Peierls, 1971).

The energy lost by the incident proton is roughly proportional to the inverse square of its velocity and, therefore, as the proton slows down, the rate of energy deposition increases. The greatest loss of energy occurs at the end of the proton range and this causes a peak at the end of the range which is called the Bragg peak. An example of a Bragg peak for a 200 MeV proton in water is shown in Figure 2.6 (Jones and Schreuder, 2001). The width of the peak is caused by a phenomenon called range straggling, which occurs due to the statistical variations in the ionization processes. In other words, not all the protons will stop at the same range as there are statistical differences in ionization processes and this spreads out the depth at which the proton beam stops. In addition, the energy of the incident proton beam is never completely monoenergetic and this also leads to spreading out of the Bragg peak.

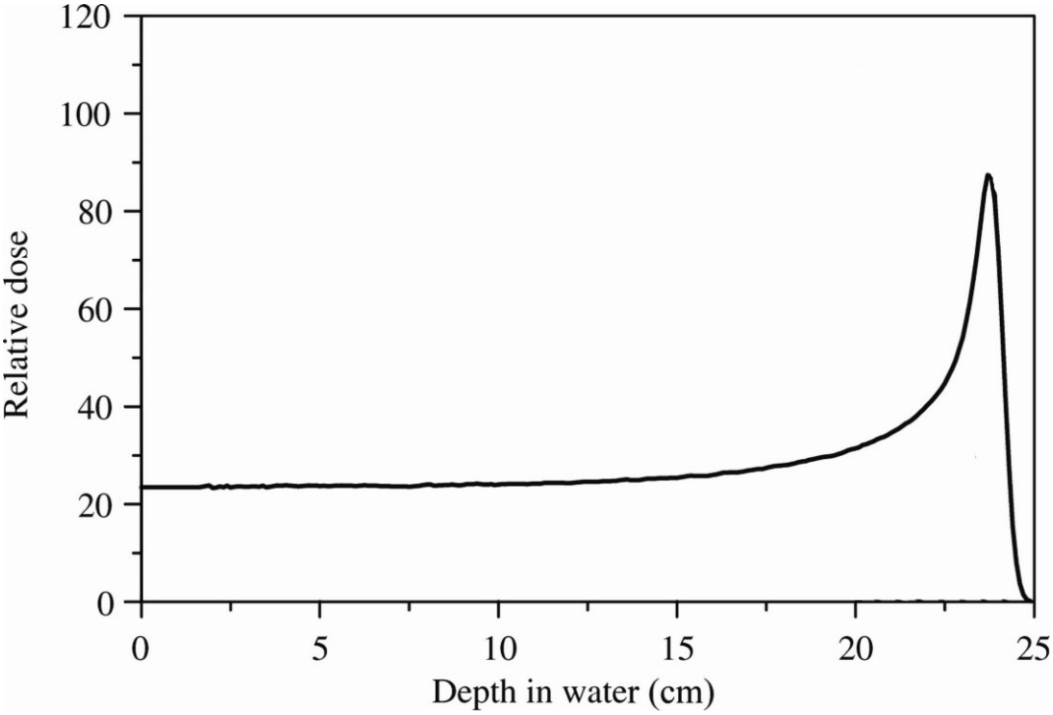

Figure 2.6: A Bragg peak for 200 MeV proton beam in water (Jones and Schreuder, 2001) .

2.4 *Spread out Bragg peak*

Usually, the width of the Bragg peak of a proton beam is not wide enough to completely cover a tumor. Therefore, the Bragg peak needs to be spread out in depth to completely cover the whole tumor volume. The enlargement of the peak dose region of Bragg peak is known as spread out Bragg peak (SOBP) in proton radiotherapy.

Figure 2.7: A common range modulator wheel used in proton radiotherapy. Picture taken from (Schlegel et al., 2006).

Multiple Bragg peaks are combined together to enlarge the peak to deliver uniform dose to the treatment volume. The desired SOBP is achieved by running the proton beam through an appropriate range modulator. A modulator wheel consists of absorbers of variable thicknesses on a circular disk as shown in Figure 2.7. A combination of low-Z (lexan or carbon) and high-Z (lead) material is used in a modulator wheel (Schlegel et al., 2006). The low-Z material is used to slow down the beam with little scattering, whereas the high-Z material is used to adjust the scattering at each depth. Each absorber thickness of the range modulator, contributes to an individual Bragg peak and the increasing widths of the absorber

leads to Bragg peaks of decreasing depths as shown in Figure 2.8. Each Bragg peak is assigned with a weight factor and a series of such Bragg peaks is finally weighted to create the desired SOBP (Schlegel et al., 2006). An example of weighted SOBP for maximum energy of 200 MeV proton beam, composed of different Bragg peaks using a range modulator, is shown in Figure 2.8.

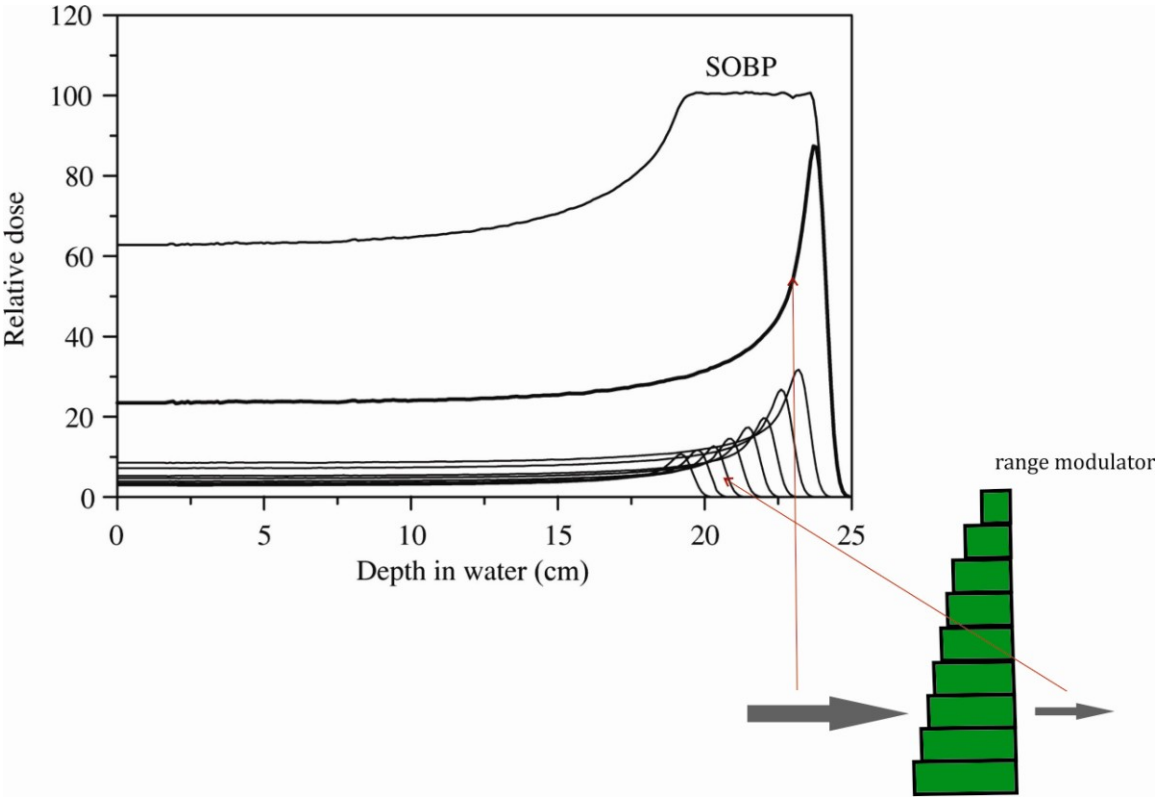

Figure 2.8: Illustration of the SOBP production using a range modulator for the maximum 200 MeV proton energy (ICRU, 2007).

As shown in the figure, at each step of the range modulator, each Bragg peak corresponds to a particular depth and weight. The total SOBP is finally created by combining the individual Bragg peaks according to their respective weights.

2.5 *Beam Delivery Techniques*

In order to conform the dose distribution to the tumor, the proton beam must be correctly shaped both laterally and longitudinally by the beam delivery system before it is applied to the patient. Currently, there are two types of beam delivery systems available: passive scattering and active scanning. In proton radiotherapy, active scanning method is considered to have the following advantages over passive scattering method (Albertini, 2011): a) it may not require a patient aperture or range compensator to achieve dose conformity, thereby minimizing exposure to secondary radiation, b) it requires less protons than passive scattering to achieve a total dose in a given volume, so less dose is delivered to the normal tissue, and c) it is considered to be more flexible in clinical use.

2.5.1 Passive Scattering

Passive scattering method is the most common beam delivery system used in proton radiotherapy (Zheng et al., 2007a). Passive scattering systems may use either a single scattering method or a double scattering method to treat the patient. In the single scattering method, a single piece of high-Z material (lead) is used to spread the beam laterally, whereas in double scattering technique a second scatterer is used further downstream to scatter the central part of the beam as shown in Figure 2.9. The second scatterer may consist of bi-material scatterers: a combination of low and high-Z materials. In the single scattering method, only 10% of the beam remains

within the central uniform region, making the single scattering method efficient only for small field size. For larger field size, efficiency is improved by the double scattering method, where up to 45% of the beam remains within the central region (Gottschalk, 2004). If a small field is required for delivering dose, single scattering method is preferred and for relatively larger fields, double scattering method is preferred (Goitein, 2008). Both types of scattering methods are currently in use in proton radiotherapy.

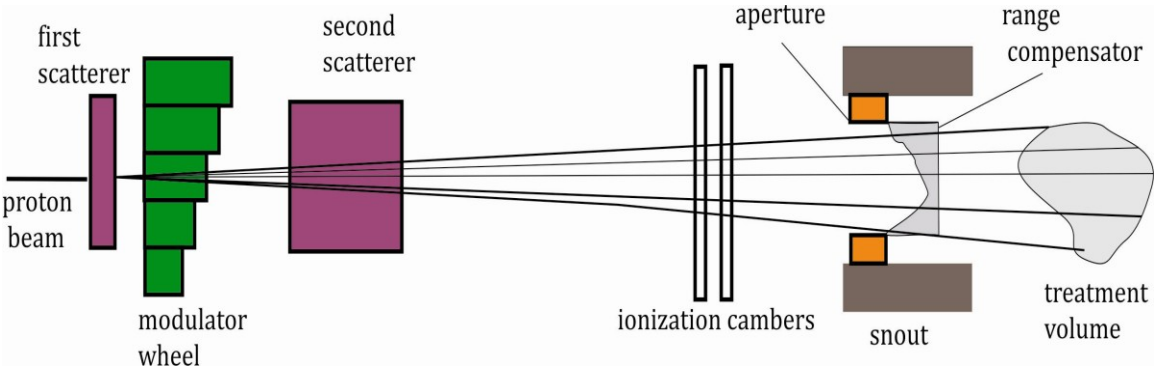

Figure 2.9: Schematic diagram of passive scattering system for proton radiotherapy.

As shown in Figure 2.9, when the beam enters the delivery system, it passes through the first scatterer, the range modulator wheel, the second scatterer, ionization chambers and finally the patient aperture and range compensator. The first and second scatterers spread out the beam laterally, while the range modulator spreads the beam in depth. The ionization chambers monitor the beam flatness, symmetry as well as the amount of delivered dose. Finally, the aperture and the range compensator conforms the proton beam to the treatment volume.

The aperture and range compensator is placed in a removable device called a snout (Figure 2.9). The snout is attached at the end of a fixed beam delivery system. Depending on the treatment field size, various types of snouts are available in proton radiotherapy. For example, the ProCure proton treatment center, Oklahoma City, OK, currently employs three snouts: snout10, snout18, and snout25 (Zheng et al., 2012). The number of each snout corresponds to the diameter of the maximum field size attainable using that snout, i.e. snout10, snout18, and snout25 corresponds to a maximum field size of 10, 18, and 25 cm diameter circular field, respectively.

The aperture shapes the treatment field to a desired target profile. This is a custom made patient specific tool designed according to the shape of the treatment volume. Generally, apertures are made of brass. The distal part of the dose deposition is shaped using patient specific range compensator. Usually, range compensator is made out of plastic to adjust the range of the protons to the distal end of the treatment volume. A custom patient aperture and a range compensator is shown in Figure 2.10. The combination of patient aperture and range compensator is used to shape the beam according to the patient treatment volume.

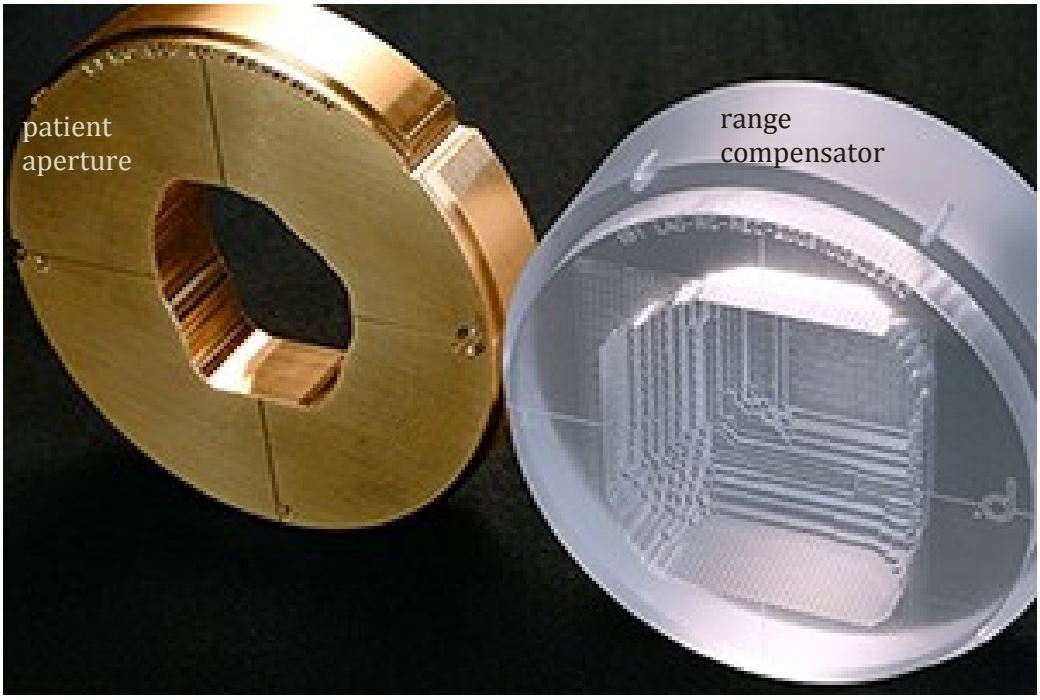

Figure 2.10: A custom patient aperture (left), and a custom made range compensator (right). Picture taken from (Decimal, 2013).

2.5.2 Active Scanning Technique

An alternative to the passive scattering method is active scanning. This was first suggested by Kanai et al. (Kanai et al., 1980) and has subsequently been implemented at different facilities around the world (Albertini, 2011). Active scanning system uses magnetic fields to deflect the proton beam over the treatment volume (Albertini, 2011). Scanning magnets are used for the necessary magnetic field required to scan the beam in the x-y plane perpendicular to the beam direction (Farr et al., 2008). The scanning in depth (z direction) to the treatment volume is done by means of energy variation. Combining the scanning ability and energy

variation, the Bragg peak can then be effectively placed anywhere inside the tumor volume.

Active scanning systems are classified into two categories (Zheng et al., 2012): a) pencil beam scanning, and b) uniform scanning. The basic differences in pencil beam scanning and uniform scanning are the following: 1) pencil beam scanning employs beam of variable intensity during scanning while uniform scanning employs a beam of uniform intensity, 2) pencil beam scanning generally does not require any patient specific aperture (Goitein, 2008) such as collimator and range compensator, while uniform scanning system uses patient specific aperture and range compensator.

2.5.2.1 Pencil beam scanning

In pencil beam scanning, a pencil beam (few mm narrow) of variable intensity is used to scan different planes (layers) of the treatment volume using sweeping magnets. The irradiation as a function of depth is done by means of changing beam energy. A schematic diagram of a pencil beam scanning system is shown in Figure 2.11. In this method, the beam starts by irradiating the deepest layer of the target and is scanned over that layer. The energy is then reduced such that the beam stops in relatively shallower layer and is then scanned over that layer. This process continues until the proximal end of the target is covered.

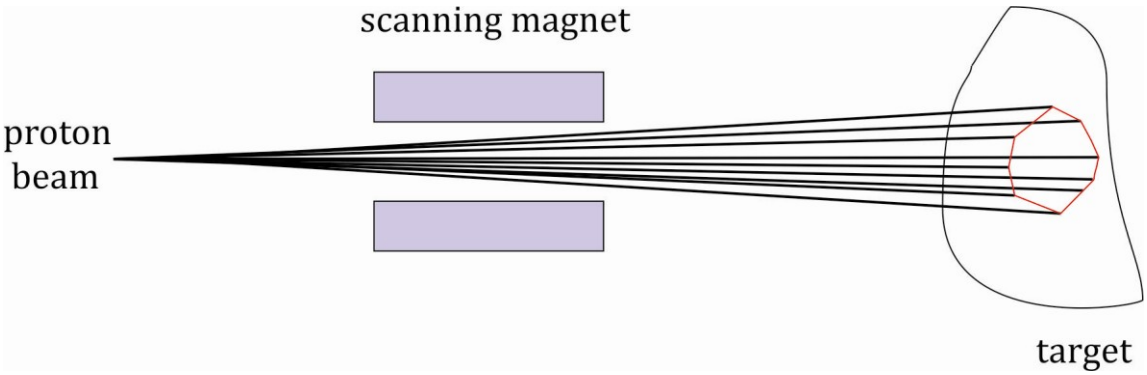

Figure 2.11: Schematic diagram of spot scanning delivery system in proton radiotherapy.

The scanning part can be done primarily in two different modes: spot scanning and raster scanning or continuous beam scanning (Schlegel et al., 2006). In spot scanning, the dose is delivered to a given spot of a particular layer of the target in a predetermined pattern at constant magnetic settings (Kanai et al., 1980). The beam is then turned off and magnetic settings are changed to irradiate the next spot. The process continues until all the predetermined spots of all layers are covered. The raster scanning or continuous beam scanning is very similar to spot scanning method except that the beam is not turned off while moves to the next spot of the target.

2.5.2.2 Uniform scanning

In a uniform scanning system, a beam of uniform intensity is scanned over different layers of the treatment volume. A schematic diagram of a uniform scanning IBA system (Louvian-la-neuve, Belgium) is shown in Figure 2.12. When the proton beam enters the beam delivery system, it passes through a first scatterer, a range

modulator wheel, the magnetic fields of the scanning magnets, ionization chamber and finally the patient aperture and range compensator. The first scatterer enlarges the beam spot and the combination of first scatterer and range modulator wheel lowers the beam energy according to the need. The modulator wheel rotates from layer to layer and allows the beam to penetrate to a particular depth of a tumor. The sweeping magnets deflect the beam by sweeping back and forth, creating a pattern of uniform intensity (Zheng et al., 2012). The ionization chambers monitor the beam uniformity, symmetry as well as the amount of delivered dose. Finally, the beam passes through a patient aperture and a range compensator contained in a snout. The combination of patient aperture and range compensator conforms the beam to the tumor shape and adjusts the proton range to the distal end of the tumor. Like pencil beam scanning, the uniform scanning system irradiates the target volume with the most distal layer of the target, then moves on to the next shallower layer. The process continues until the proximal edge of the target is covered.

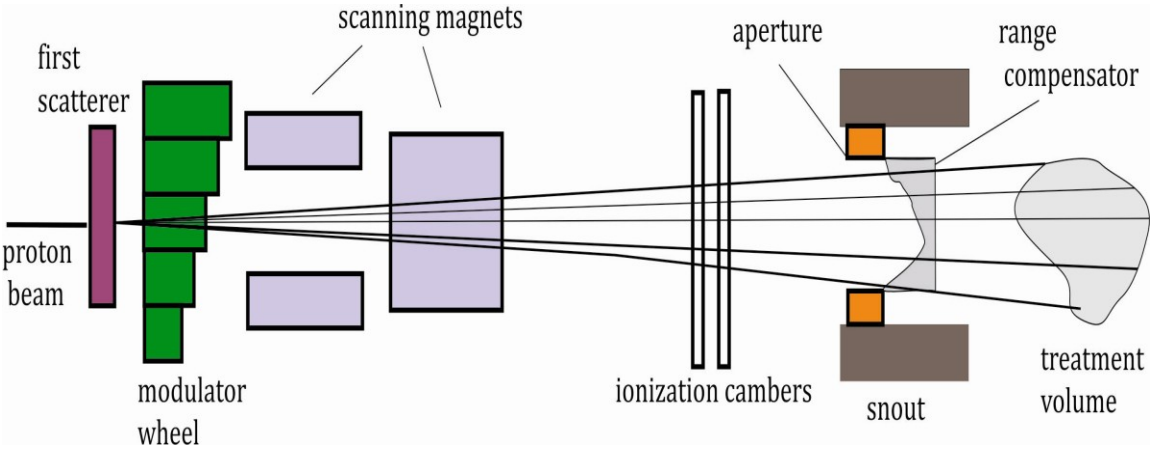

Figure 2.12: Schematic diagram of IBA uniform scanning nozzle. The components in the nozzle is not in scale.

The study reported on in this work determined the dose equivalent from secondary neutrons produced by a uniform scanning system. It is important to note that uniform scanning devices use similar beam shaping components (aperture and range compensator) as used in passive scattering systems. The difference is that no second scatterer is used in uniform scanning systems.

2.6 *Secondary Neutron Production*

In proton radiotherapy, the primary proton beam is shaped using different beam shaping devices: scatterer, range modulator, patient collimator and range compensator. The interaction of the proton beam with these devices is likely to produce secondary particles through non-elastic nuclear interactions (Brenner et al., 2009). The production of secondary particles depends on the type of material and the energy of the incident protons. These secondaries may consist of different

types of particles including neutrons, electrons and alpha particles. Of these secondary particles, neutrons are the most potentially damaging as they possess a high relative biological effectiveness (RBE). Exposure to secondary neutrons of healthy tissue outside the target volume may lead to a secondary cancer later in the life of the patient (Hall and Giaccia, 2006). Apart from the beam shaping material, the patient's body itself can generate a fair number of secondary neutrons (Dowdell, 2011). Since these neutrons are created inside the patient, some exposure of healthy tissue to secondary neutrons is unavoidable.

The level of secondary neutron production depends largely on the beam delivery system since each beam delivery system uses different beam shaping components. Among them, the patient specific aperture is considered to be the dominant contributor of secondary neutrons to patient dose received otside the treatment volume (Jiang et al 2005, Mesoloras et al 2006, Zheng et al 2007, Zacharatou Jarlskog et al 2008, Perez-Andujar et al 2009). It is important to note that, in all cases, the field size is larger than the patient specific aperture (Brenner et al., 2009). This is due to the limited number of field sizes the accelerator can produce. This overlap in field size and aperture, along with the continual scanning of the beam until the prescribed dose to the treatment volume is met, will produce secondary neutrons.

The neutrons produced by protons in the energy range of 65 to 250 MeV are the result of two nuclear processes: a) intranuclear cascade, and b) nuclear evaporation.

A graphical illustration of the intranuclear cascade process and evaporation process is shown in Figure 2.13. The intranuclear cascade process is particularly important for proton energies greater than 50 MeV (Benton, 2004). The process takes place when incident particles interact with the nucleons of a target nucleus and produce protons, neutrons, alpha particles and occasionally heavier nuclei at lower energy but at wider angles (Figure 2.13). The emission of these particles during an intranuclear cascade occurs usually in the forward direction, i.e. in the direction of the primary beam. The particles emitted due to intranuclear process can undergo additional nuclear interactions which are called extra nuclear cascades. The probability of an extra nuclear cascade in proton radiotherapy is small as the energy required for such events is greater than a few hundred MeV. The neutrons produced due to intranuclear cascades start from about ~10 MeV and can be as high as the incident proton energy (Zheng et al., 2007a).

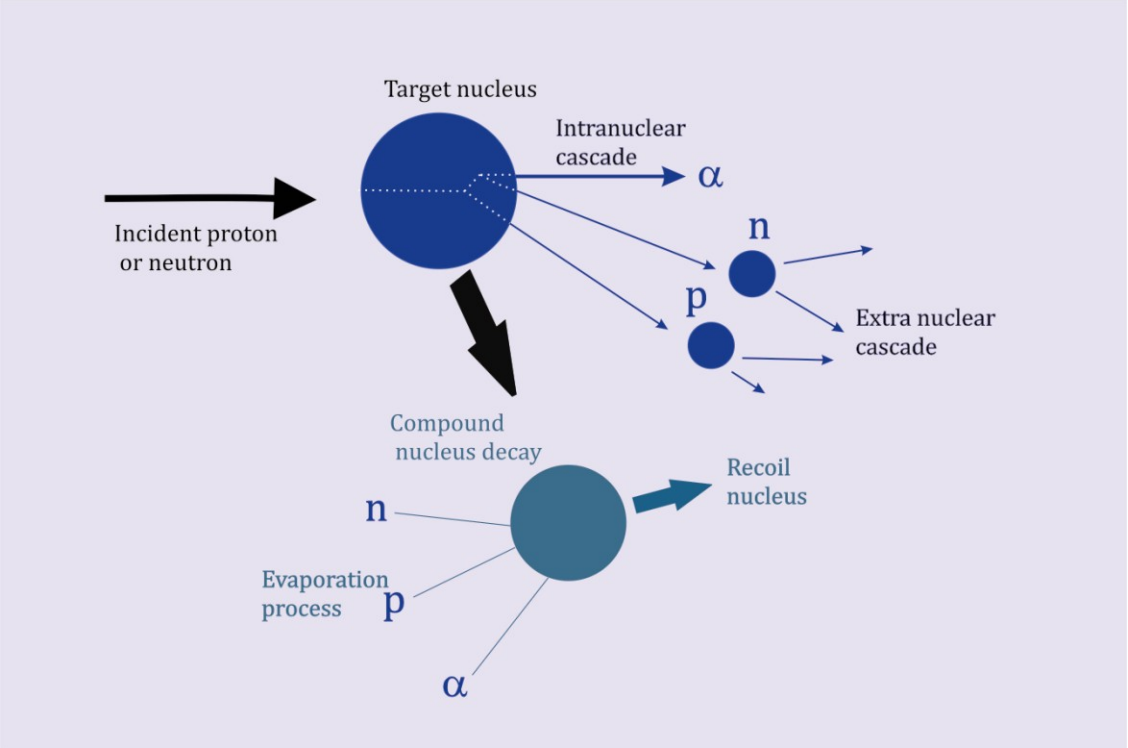

Figure 2.13: Illustration of intranuclear cascade and evaporation process.

The evaporation process, on the other hand, occurs in a multi-step processes. After the initial collision by an incident proton and a following intranuclear cascade, the target nucleus is often left in an excited and unstable state (Figure 2.13), commonly referred as compound nucleus (Benton, 2004). The nucleus can de-excite and achieve stability through the evaporation of neutrons, protons, and alpha particles. The emission of these particles by the evaporation process is nearly isotropic. Neutrons emitted as a result of evaporation process range in energy from 0 to 10 MeV (Zheng et al., 2007a).

2.7 *Secondary neutron interaction with matter*

A neutron can interact in a number of ways with a nucleus. The probability of such an interaction is expressed in terms of cross section (Rinard, 1991), having dimensions of area, i.e. cm^2. In nuclear physics, cross section is often given in units of barns (1 barn equals to 10^{-24} cm^2). Depending on the energy of the neutron and the type of target nucleus, various types of interactions (Figure 2.14) are possible. The total cross section represents the probability of any such interactions.

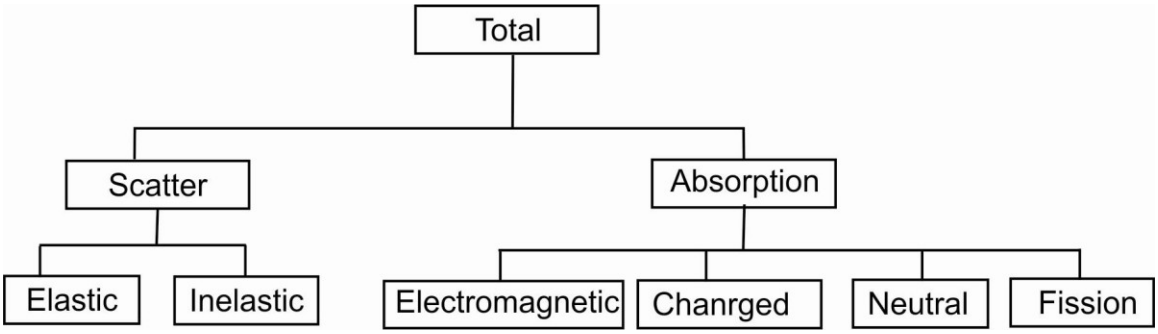

Figure 2.14: Different types of neutron interaction.

Generally, two major types of neutron interaction are possible with matter: a) scattering, and b) absorption. In scattering interaction, a neutron is scattered by a target nucleus where the direction and speed of the incident neutron changes, but the target nucleus is left intact. Scattering events are further divided into two categories: elastic, and inelastic scattering. In elastic scattering, the total kinetic energy of the event is conserved and the internal state of the target nucleus and neutron remains unchanged. In inelastic scattering, the total kinetic energy is not

conserved because the target nucleus undergoes some internal arrangement that eventually leads to the emission of radiation (Rinard, 1991).

In the absorption process, a neutron is absorbed by the target nucleus. As shown in Figure 2.14, due to the absorption, a wide range of emission may occur or fission may be induced. When a neutron is absorbed by a target nucleus: a) the target nucleus may move to higher excited state and the de-excitation may lead to the emission of electromagnetic radiation i.e. gamma rays, b) emission of charged particles like protons, deuterons and alpha particles may take place, c) neutral particles (neutrons) may be emitted, and d) a fission event, i.e. the nucleus to splits into two or more fragments and a number of neutrons may occur (Rinard, 1991).

Total cross section of a neutron depends on its incident energy. Neutrons are classified into four groups based on their energy: fast neutrons (> 500 keV), intermediate neutrons (10 keV-500 keV), epithermal neutrons (0.5 eV-10 keV), and thermal or slow neutrons (< 0.5 eV). Fast and intermediate neutrons, in general, undergo scattering interaction while thermal or epithermal neutrons undergo absorption interaction.

2.8 *Total cross section of secondary neutrons on tissue*

The total cross section of neutrons on tissue largely depends on the interaction of neutron with hydrogen, carbon, and oxygen since they are the most common

elements in human body. Fast neutrons (> 1 MeV) interact with carbon and oxygen nuclei in tissue through inelastic process and can release alpha particles (Figure 2.15) (Hall and Giaccia, 2006). These alpha particles deposit dose to the tissue. Intermediate energy neutrons (10 keV-500 keV) transfer energy to the tissue via elastic scattering with the nuclei (protons) of hydrogen atoms. In this process, an incident neutron elastically scatters off by hydrogen nucleus transferring energy and creating a recoil proton (Figure 2.16). Thermal neutrons (< 0.5 eV) transfers energy through absorption process.

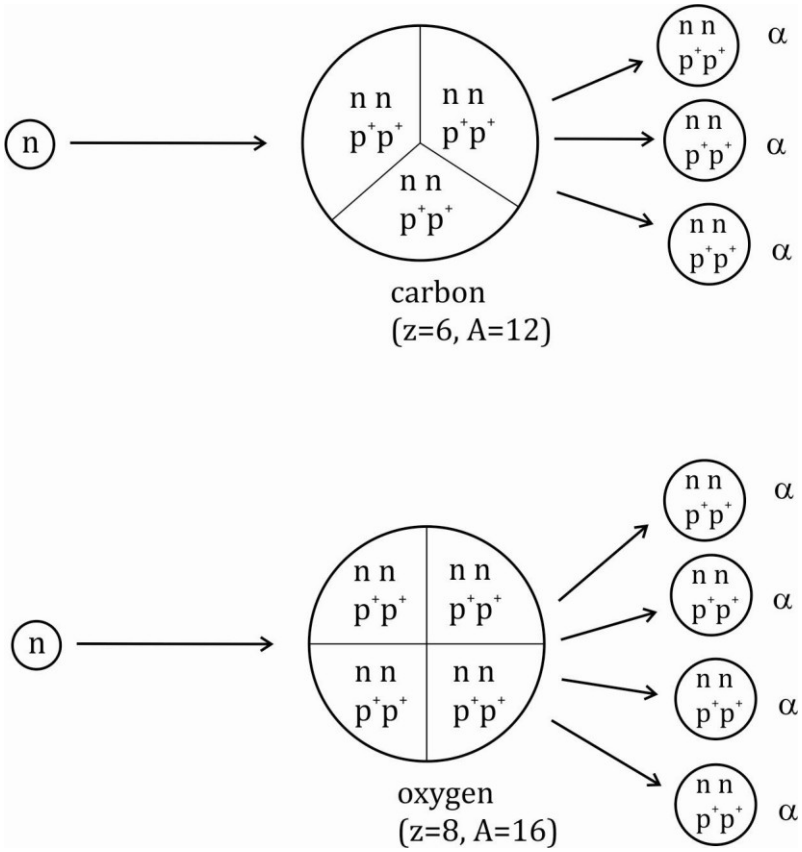

Figure 2.15: A schematic representation of neutron interaction with carbon (top), and oxygen (bottom) nucleus, results three and four alpha particles respectively. Picture taken from (Hall and Giaccia, 2006).

Among different interactions, neutron interaction with hydrogen nuclei via elastic scattering is considered the dominant mechanism of energy transfer to soft tissue (Howell, 2010). The reasons for this are: a) hydrogen is the most abundant element in tissue, b) the similar mass of a proton and a neutron allows maximum energy to be transferred in elastic scattering, and c) hydrogen possesses a large elastic scattering cross section for neutrons (Hall and Giaccia, 2006).

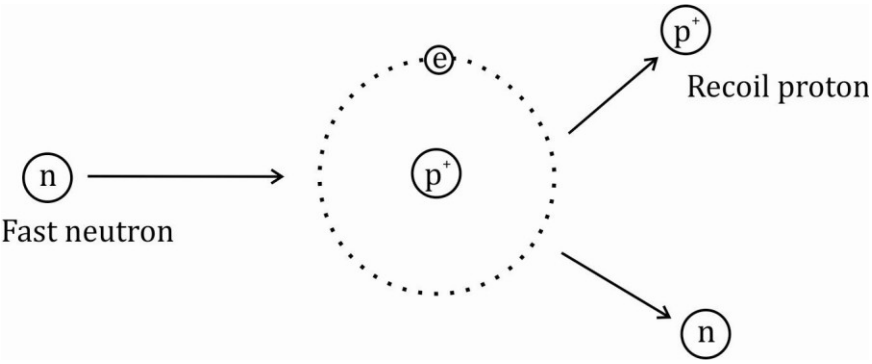

Figure 2.16: A schematic representation of fast neutron's interaction with hydrogen atom inside tissue (Hall and Giaccia, 2006).

Total cross sections for incident neutrons (energy up to 20 MeV) on hydrogen, carbon and oxygen are shown in Figure 2.17 (NNDC, 2013). This figure shows that the total cross sections for neutrons on carbon, hydrogen and oxygen are either decreasing or constant with energy due to inelastic and elastic interactions, respectively. The resonance peaks (around 0.1 to 10 MeV) are present for carbon and oxygen but not for hydrogen.

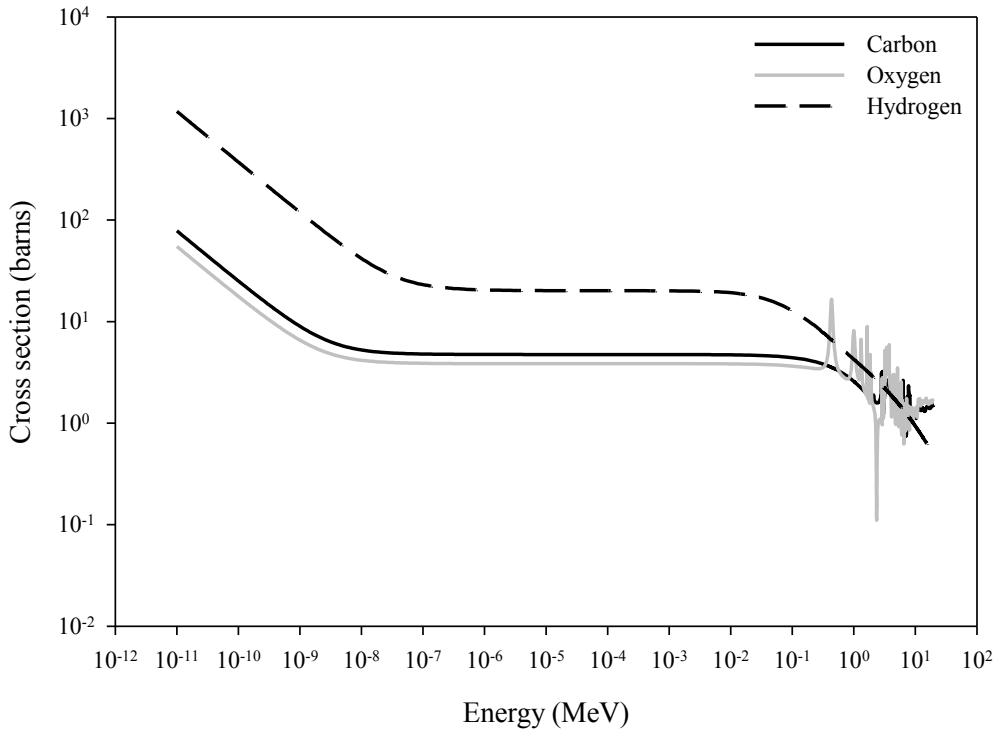

Figure 2.17: The average total cross section of neutron for carbon, oxygen and hydrogen as a function of incident neutron energy (NNDC).

Figure 2.17 shows that the average total cross section for hydrogen is about an order of magnitude greater than that of carbon and oxygen, for the identical neutron energy. The hydrogen content in tissue, therefore, dominates the neutron response. For this reason and because of the similarity of the atomic mass percentage (Table 2.2) of hydrogen in both, water and tissue (ICRU muscle), this study considers water for the study of neutron response on tissue. Also in radiation therapy, water is considered to be a standard replacement of tissue for beam commissioning, machine calibration, or patient dose verification (Das et al., 2008).

Table 2.2: Atomic percentages for ICRU muscle (Collums, 2012) and water.

Content	Atomic percentages (%)	
	ICRU muscle	water
H	63.3	66.67
C	6.4	
O	28.5	33.33
other	1.8	

The total cross section as a function of neutron energy on water and ICRU muscle is shown Figure 2.18. The negligible difference of neutron average total cross section on water and tissue (ICRU muscle) demonstrate that the water is a reasonable replacement of tissue for neutron study.

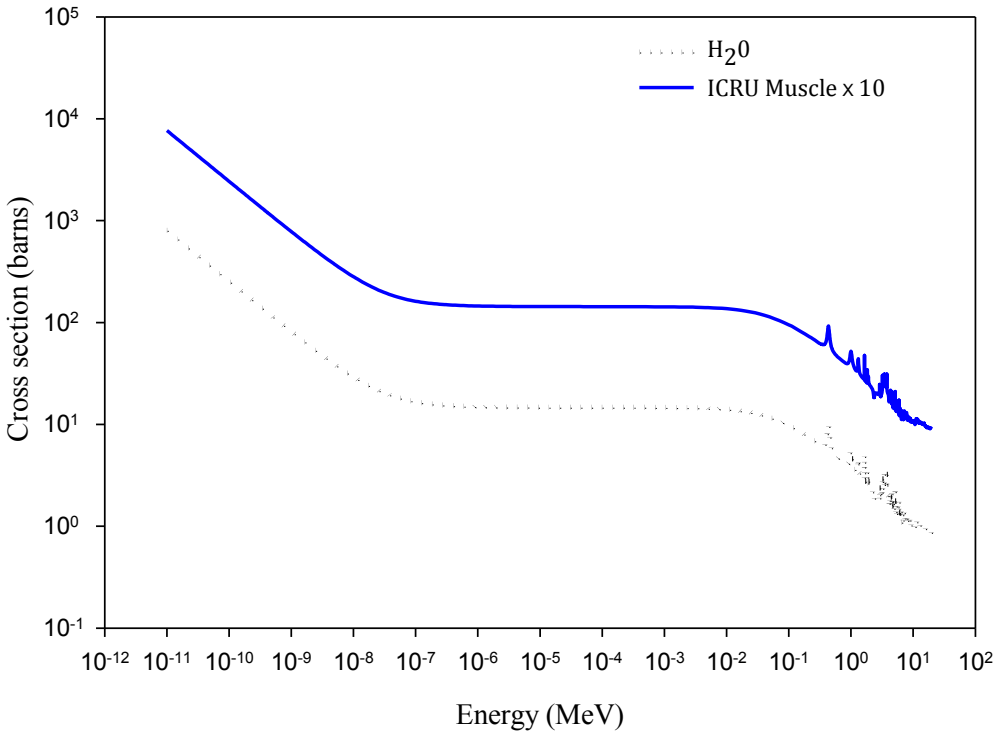

Figure 2.18: The average total cross section of neutron for ICRU muscle and water as a function of incident neutron energy(NNDC, 2013). ICRU muscle cross section is multiplied by 10 in the graph for clarity .

CHAPTER 3

DOSIMETRIC QUANTITIES

This chapter describes the dosimetric quantities including particle fluence, LET (linear energy transfer), dose and dose equivalent. The fluence to dose conversion coefficients used in FLUKA is described. A standard guideline for radiation leakage in radiation therapy is also mentioned.

3.1 *Particle Fluence*

According to the international commission of radiation units and measurements (ICRU), particle fluence, Φ, is defined as the number of particles, dN, that cross a unit area, dA (ICRU, 1998a):

$$\Phi = \frac{dN}{dA}. \tag{3.1}$$

The SI unit of particle fluence is particles/m^2. For isotropic or nearly isotropic situations, fluence is corrected for solid angle, Ω:

$$\Phi = \frac{dN}{dAd\Omega}, \tag{3.2}$$

where the unit is cm^{-2}sr^{-1}.

3.2 *Linear Energy Transfer (LET)*

Linear energy transfer (LET) is the energy deposited per unit path length when a particle passes through a medium. LET depends on both the type of radiation and the target material. LET is determined by the rate of energy loss in the medium:

$$LET = \frac{dE}{dl} \tag{3.3}$$

where dE denotes the energy loss in the length, dl, of the stopping medium. The SI unit for LET is Joules/meter, though in radiation dosimetry LET is commonly expressed in keV/μm.

LET is related to quantities like mass stopping power and linear stopping power. The mass stopping power is similar to linear stopping power except that it is independent of density of the material. According to the ICRU (ICRU, 1998b), the mass stopping power, $\frac{S}{\rho}$, is

$$\frac{S}{\rho} = \frac{1}{\rho}\frac{dE}{dl}, \tag{3.4}$$

where, S, is linear stopping power and ρ is the density of the material. The SI unit of mass stopping power is J.m^2/kg but in practice mass stopping power is usually expressed as MeV·cm^2/g. The linear stopping power primarily accounts for the energy loss due to atomic collisions (electronic loss) and can be estimated using the Bethe-Bloch formula.

3.3 *Absorbed dose and dose equivalent*

Absorbed dose refers to the amount of energy absorbed per unit mass of material as a result of radiation exposure and can be expressed as:

$$D = \frac{dE}{dm}, \tag{3.5}$$

where, *dE* is the energy absorbed in the mass, *dm,* of the material. The SI unit of the absorbed dose is the Gray (Joule/Kg). The absorbed dose can be calculated as:

$$D = \frac{1.602 \times 10^{-9}}{\rho} \Phi * \text{LET}, \tag{3.6}$$

where Φ is he fluence and ρ is the density of the material and the factor 1.602×10^{-9} converts the keV to joules. Equation (3.6) represents dose for a monoenergetic beam, i.e. all particles possess one fixed LET. For a mixed field, the LET of each type of radiation and energy needs to be considered:

$$D = \frac{1.602 \times 10^{-9}}{\rho} \sum_{n} \Phi_n * \text{LET}_n, \tag{3.7}$$

where, the subscript "*n*" accounts the type of the radiation and energy, and Φ_n and LET_n are the corresponding fluence and LET, respectively.

Dose equivalent estimates the biological damage due to the absorbed dose in matter. The International Commission on Radiological Protection (ICRP) defines dose equivalent as the product of the absorbed dose and LET dependent quality factor, Q (LET):

$$H = Q(\text{LET}) * D. \tag{3.8}$$

The SI unit of dose equivalent is the Sievert. The quality factor, Q, has been adopted from annex A of ICRP Publication No. 60 (ICRP, 1991) as shown below:

$$Q(LET) = \begin{cases} 1.0, & \text{LET} < 10 \text{ keV/µm} \\ 0.32LET - 2.2, & 10 \text{ keV/µm} \leq LET \leq 100 \text{ keV/µm} \\ 300/\sqrt{LET}, & \text{LET} > 100 \text{ keV/µm}. \end{cases} \tag{3.9}$$

A plot of Q value against LET is shown Figure 3.1.

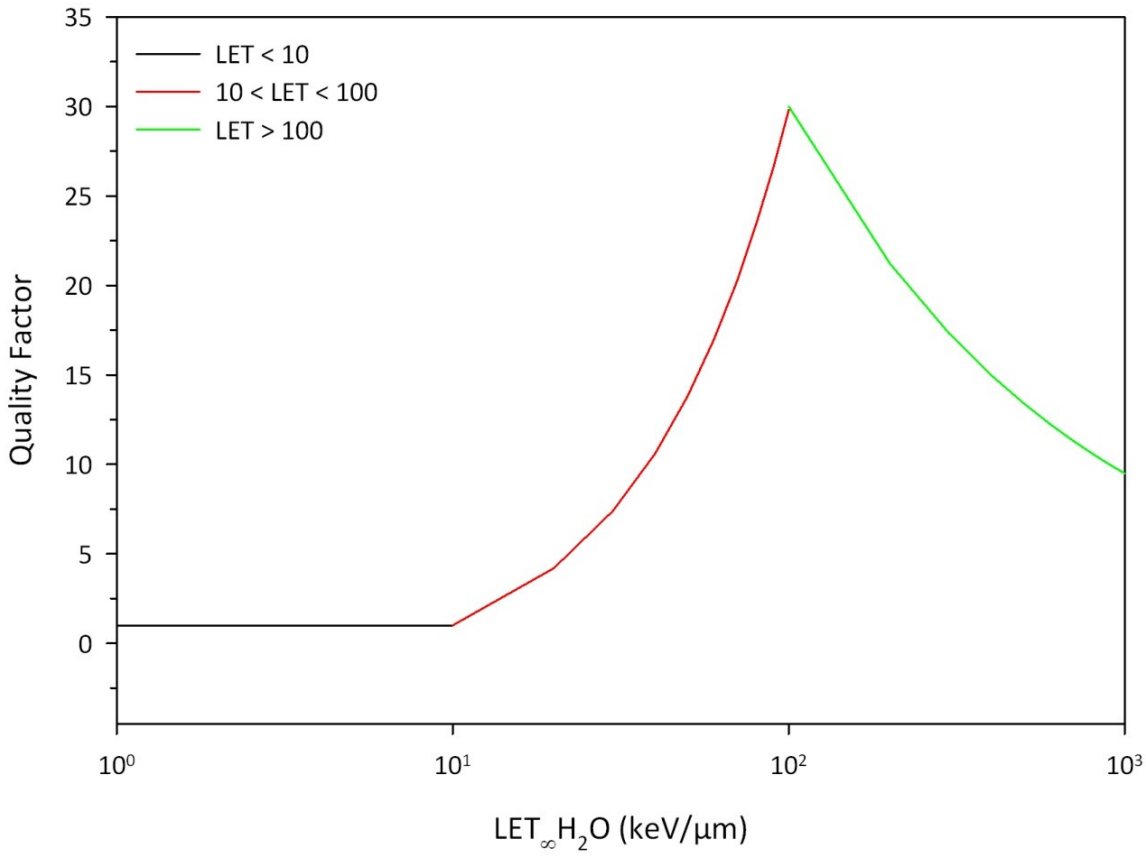

Figure 3.1**:** Quality factor, Q, as a function of LET as defined in ICRP Publication No. 60 (ICRP, 1991).

It is important to mention that the quality factor is determined based on stochastic endpoints rather than deterministic endpoints. In stochastic processes there is no

threshold for biological damage including the induction of cancer, whereas, in deterministic processes, a biological threshold is considered.

This process of determination of the absorbed dose and dose equivalent is LET dependent. However, in 1991, ICRP-60 (ICRP, 1991), introduced few new quantities to replace the LET dependent dose equivalent. The first of these quantities is the equivalent dose, H_T:

$$H_T = \sum_R w_R * D_{T,R,} \tag{3.10}$$

where $w_R$is the radiation weighting factor and depends on the energy and type of the incident radiation and $D_{T,R}$ is the absorbed dose average over the specific tissue or organ, *T*, by the radiation, *R.* The ICRP-60 defined weighting factors are shown in the Table 3.1.

Table 3.1: Radiation weighting factor, w_R, as defined in ICRP-60 (ICRP, 1991) for neutron of different energy range.

Energy	w_R
<10 keV	5
10 keV to 100 keV	10
>100 keV	20
2MeV to 20 MeV	10
>20 MeV	5

The second quantity is the effective dose, E:

$$E = \sum_{T} w_T * H_{T,} \tag{3.11}$$

where w_T is the weighting factor for the tissue, T, and H_T is the equivalent dose. The effective dose represents the sum of the weighted equivalent doses in all tissues and organs of the human body. The weighting factor w_T is available at ICRP-60.

FLUKA calculates dose equivalent using fluence to dose equivalent conversion coefficients. The coefficients are determined based on radiation weighting factor, $w_{R,}$ and are described at ICRP publication No 74 (ICRP, 1996). A spline fits to the conversion coefficients of ICRP publication No 74 (ICRP, 1996) was employed in the code. Also a separate conversion coefficients was calculated by Pelliccioni (Pelliccion, 1998) and implemented in the FLUKA code for higher energy of neutrons (Roesler and Stevenson, 2006). The fluence to dose equivalent conversion coefficients for ICRP74, Pelliccioni and the fitted curve (AMB74) is shown in the Figure 3.2. FLUKA employs the fitted curve AMB74 (shown by red line) and the coefficients determined by Pelliccioni (shown by blue diamond) in the dose equivalent calculation.

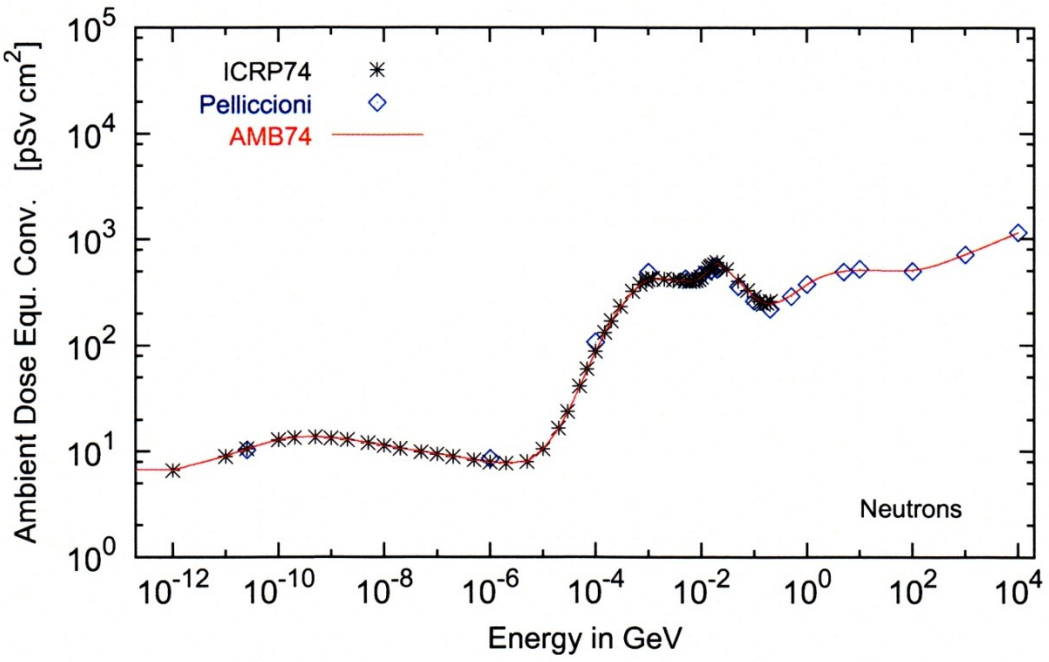

Figure 3.2: Ambient dose equivalent coefficients as a function of neutron energy. Plot taken from (Roesler and Stevenson, 2006).

3.4 *Guidelines to leakage Radiation Exposure*

Currently, there are no active regulations or guidelines for the radiation leakage from proton or heavy ion therapy unit (Moyers et al., 2008). However, different states in the USA have their own states regulations for radiation therapy. Most therapy facility still follows the recommendations made by the American Association of Physicists in Medicine (AAPM) task group for electron and x-ray therapy. In 2006, the International Electro-Technical Commission (IEC) recommended that the physical dose due to leakage of primary particles downstream of beam line should be within 2% of prescribed dose (Moyers et al., 2008). But no recommended dose for neutrons was mentioned. It should be noted

that neutron energy and fluence vary from proton radiotherapy center to center and depends on the beam delivery technique. Also, the existing literature (Moyers et al., 2008) supports the view that the published data on secondary neutrons in proton radiotherapy is not adequate for making any conclusive recommendation on neutron exposure. However, since neutrons possess a higher RBE and the neutron exposure could lead to secondary cancer later in the patient's life, the absorbed dose from neutrons should be as low as possible (Hall, 2006).

CHAPTER 4

FLUKA SIMULATIONS

4.1 *Monte Carlo Code FLUKA*

The term Monte Carlo refers to the repeated random sampling technique, where a physical event is simulated by observing the probable behavior of that system from the outcome of a large number of trials. Each of the trial is played on a computer by a sequence of random numbers. With the help of random numbers, this method simulates a physical problem via probabilistic approach. Therefore, this is sometimes called a virtual experiment.

An illustration of the Monte Carlo method in the radiation transport is shown in Figure 4.1 for an isotropic monoenergetic neutron source placed inside a shielding sphere. The trajectory of each neutron inside the shield is shown by succession of straight lines whose lengths and directions are random relative to each other. Monte Carlo method predicts this trajectory based on the probability of neutron's interaction probability (cross section) with the shielding material. For instance, in the first step of the history, the free-path length (the path without interactions) of a neutron is determined by using a random number following the technique,

mathematical transformation. The second step is decided based on the first step i.e. in the first step if the neutron is scattered, or absorbed. If it is absorbed the history ends and if it is not absorbed the history continues until it is absorbed. The outcome of such events demonstrates how many neutrons may escape from the shielding. For example, if N is the total number of neutron history generated and n of that escapes then the probability of a neutron that escape from shielding is n/N. The statistical uncertainty of any such event is related to the number of total number of history generated in the process. The more the history generated the better the statistical uncertainty will be.

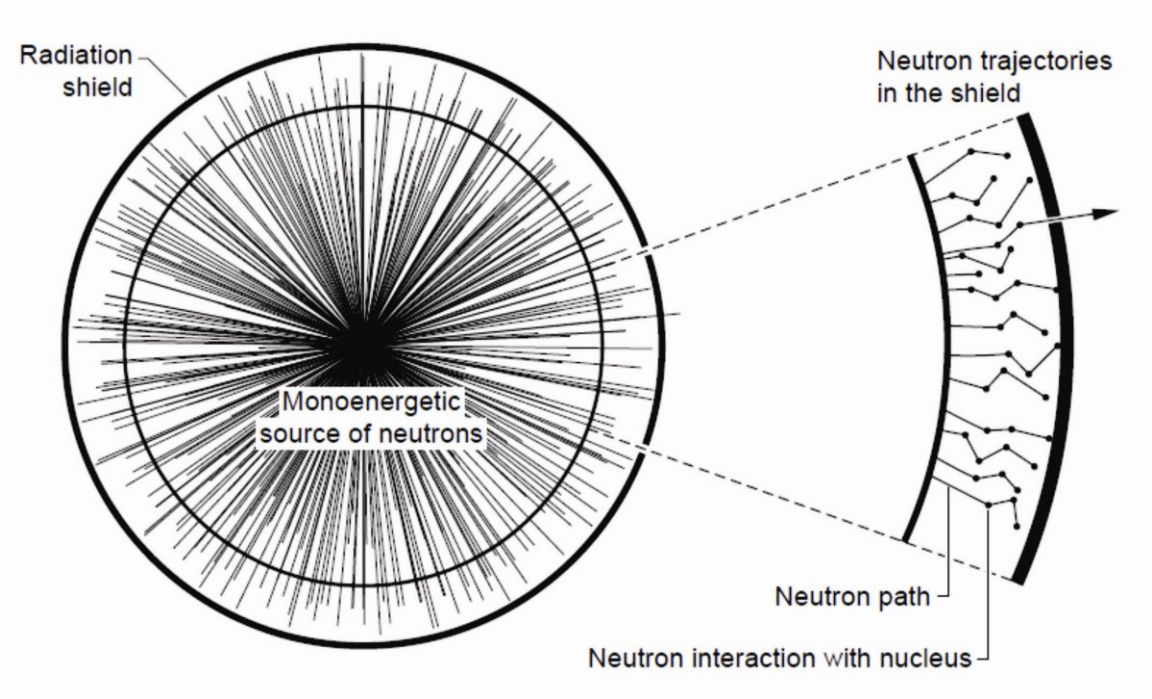

Figure 4.1: Illustration of Monte Carlo approach using an isotropic neutron source. Picture taken from (Hendricks, 1994).

This study uses Monte Carlo radiation transport code called FLUKA to study the neutron dose equivalent from uniform scanning proton beam. FLUKA is an integrated Monte Carlo simulation package which is widely used in many areas of physics, engineering including high energy experimental physics, medical physics, cosmic ray research, radiation detector design, radiation shielding design of radiotherapy units etc. (Andersen et al., 2004, Aiginger et al., 2005, Ballarini et al., 2007, Battistoni et al., 2007, Fassò et al., 2005).

FLUKA was originally developed by the European Organization for Nuclear Research (CERN) to model the secondary radiation environment produce by particle accelerators. Later the code was adapted for the predictions of dosimetric quantities in medical physics and in radiobiology. FLUKA can reproduce the interactions and propagation of about 60 different particles in matter with excellent accuracy. This code can track electrons and photons from 1 keV to thousands of TeV, hadrons of up to 20 TeV and all the corresponding anti particles including neutrons down to thermal energy. This code can also simulate polarized photons (e.g. synchrotron radiation) and optical photons. FLUKA can also track emitted radiation from unstable residual nuclei and their corresponding time of evolution. The code is developed in such a way that it can correctly model the behavior of charged particles in the presence of magnetic and electric fields.

In this study, we used FLUKA to simulate all the relevant physics that occurs when a proton beam penetrates into and passes through the complex mass distribution

represented by the beam delivery system and a phantom patient. Individual primary protons are treated through the geometrical mass distribution and at each point along proton's trajectory, the probability of different electronic and nuclear interactions is calculated and an outcome of that interaction is determined based on a weighted random number. The products of these interactions including neutrons are in turn followed through the mass distribution and the probability of interactions of these secondary particles with the mass is in turn calculated. This continues until all the particles produced as a result of the incident primary proton either stop or leave the volume of interest (i.e. enter the black hole). This calculation is repeated for a large number of primary protons so as to obtain convergence on an average with good statistics. Finally, the LET spectrum, dose, and dose equivalent are scored by adding up the outcomes of all the simulations at particular locations of interest within the volume of interest.

There are three main components in FLUKA structure: a) geometry of the problem, b) physics set up, and c) scoring. In the geometry section, the combinatorial geometry principle is used. For example, basic bodies, such as cylinders, spheres, parallelepipeds, etc. are combined to build a complex region of the problem. The combination is performed using basic Boolean operations- union, intersections and subtractions. Each region of the geometry is assigned with an appropriate material. After the geometry is built, it is mandatory to surround the geometry using a region called the "black hole". The purpose of the black hole is to stop infinite tracking of

particles, i.e. particles need to be stopped at some point. The black hole stops those particles which are no longer in the user's region of interest.

In the physics component, FLUKA employs appropriate physics to simulate particle interactions including hadron inelastic nuclear interactions, elastic scattering, nucleus-nucleus interactions, etc. FLUKA also has the capacity of transporting particles of particular range of energy. The transport of all FLUKA particles can be enabled for energies as low as 1 keV. Neutrons can be transported to energies as low as 10^{-5} eV. Secondary electron production threshold (minimum energy required to produce a secondary electron) can be as low as 1 keV for all particles and 10^{-5} eV for neutrons. A detailed description of physics and the related data which has been employed in FLUKA can be found at (FLUKA, 2013).

In scoring section, FLUKA estimates or scores the quantity of interest (e.g. dose) in the user defined region. The scored quantity is always embedded with statistical uncertainties. However, the uncertainty can be improved by increasing the number of primary particles in the simulation. In other words, by increasing the number of incident primary particles, the statistics of radiation interactions can be improved. FLUKA has built in capacity to score a great number of quantities of interest e.g. particle fluences, current, LET, track length, energy spectra, Z spectra, energy deposition, dose, dose equivalent, etc.

For the determination of dose equivalent from neutrons, FLUKA employs neutron cross sections divided into 260 energy groups (Ferrari et al., 1997) where the lowest energy group is 10^{-5} eV. The wide energy range of neutron cross sections available in FLUKA was the primary reason for using FLUKA over other available Monte Carlo radiation transport codes. FLUKA is considered a reputable Monte Carlo radiation transport code for neutron studies in proton radiotherapy (Moskvin et al., 2012, Schneider et al., 2002, Pe´rez-Andu´jar et al., 2012).

In this study, for all particles except neutrons, the transport and secondary electron threshold was set to 100 keV. This implies that all the particles except neutrons will be transported when the energy is equal to or greater than 100 keV. The particle transport and secondary electron could be decreased to 1 keV, but such a low energy threshold would significantly increase the computation time. A separate routine was compiled to score the dose equivalent from neutrons of energy 1 to 20 MeV, because the interaction cross section for water with neutrons of energy greater than 20 MeV is fairly small. The statistical uncertainty was improved by increasing the number of primaries so that the dose equivalent at each location was calculated to within a statistical uncertainty of 5%.

4.2 *Simulation of simplified snout*

A simplified snout which is in use at ProCure Proton Therapy Center, Oklahoma City, OK, was modeled using the FLUKA geometry package. The major components of the

snout which was simulated in this study were the snout base (brass), snout wall (stainless steel), and patient specific aperture (brass). Cross sectional and FLUKA geometry diagrams of the snout geometry are shown in Figure 4.2.

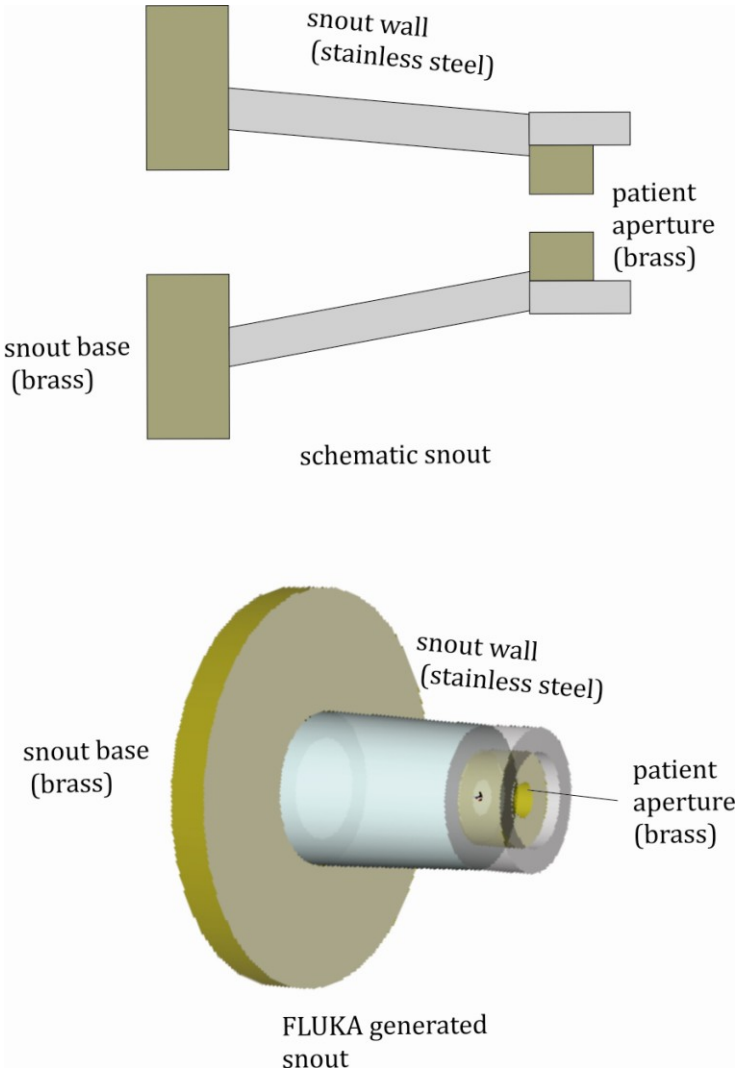

Figure 4.2: The cross sectional diagram of the snout (top), FLUKA geometry generated diagram of the snout (bottom). The snout is used at ProCure Proton Treatment Center, Oklahoma City, OK (Figure is not in scale).

The reason for using the simplified snout is that the major contributions of secondary neutrons to the patient come from the patient aperture which is housed in the snout, since it is closer to the patient than most other components in beam delivery system. A recent study has shown that patient specific aperture in proton radiotherapy contributes about 80% to 90% of the total secondary neutrons that may reach the patient (Brenner et al., 2009). This study only looks at neutrons produced in the snout and inside the phantom.

4.3 *Simulation setup*

FLUKA simulations were carried out for three proton beams of 78 MeV, 162 MeV, and 226 MeV. A common set of treatment parameters was used throughout the entire study: a 4 cm spread out Bragg peak (SOBP), a 5 cm diameter patient brass aperture, a 10 cm from surface to isocenter, a 28 cm distance from snout to surface of the phantom, a 18 x 18 cm^2 uncollimated beam, and no range compensator. A diagram of the setup is shown in Figure 4.3. As shown in the figure, a polyethylene phantom of 0.96 gm/cm^3 density was placed in front of the snout to represent a patient. The phantom was built by assembling polyethylene blocks, each having a dimension of 20 x 20 x 5 cm^3. Using these blocks, a phantom of 60 cm in length and 20 cm in width was created for the experiment. As shown in Figure 4.3, three columns of polyethylene blocks were assembled to construct the phantom along the beam direction, where the thickness of the phantom differed along the length. The thickness of the first and the third column was 35 cm, and the thickness of the second column was

52 cm to cover the 135° angled detectors. The detectors were located at 7.5 cm, 17.5 cm, 28 cm and 35 cm from the beam isocenter at 45°, 90°, and 135° from primary beam axis.

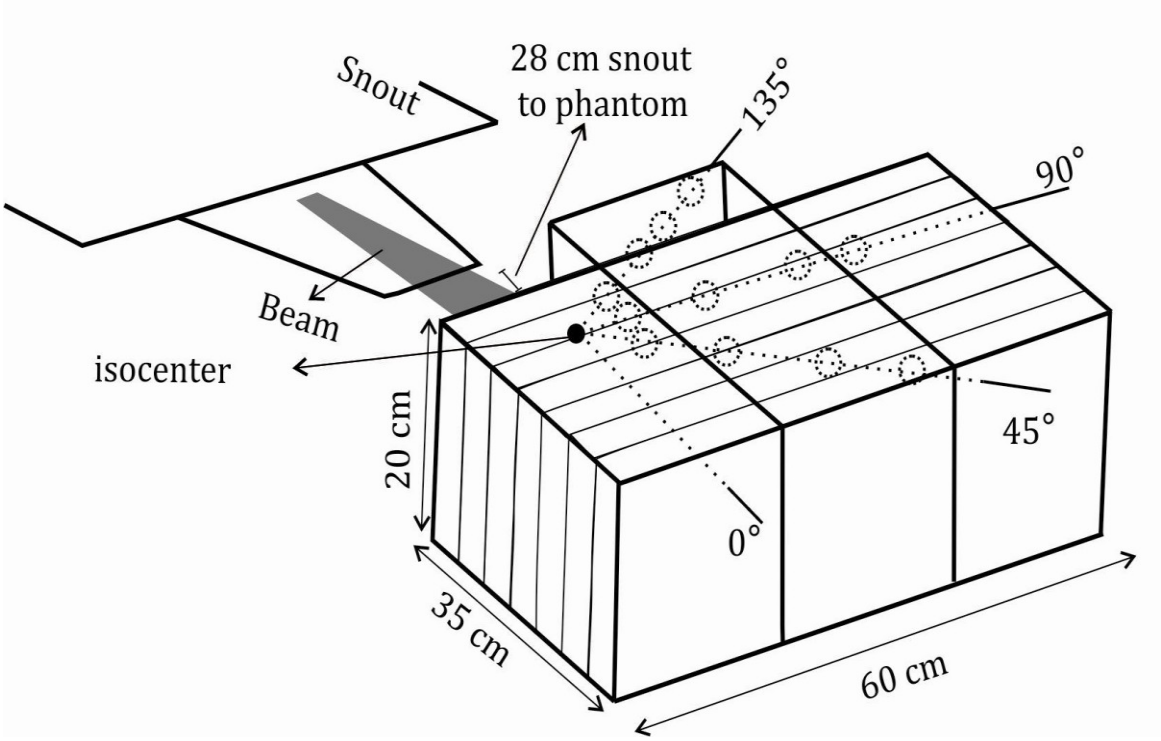

Figure 4.3: Diagram of the setup with the presence of phantom. Dotted circles represent the detectors locations where dose equivalent was calculated inside the phantom.

The dimension of each simulated detector was chosen to be 4 x 4 x 0.05 cm^3 to simulate the experiment that was performed with CR-39 plastic nuclear track detectors (PNTDs) of the same dimensions at ProCure Proton Therapy Center, Oklahoma City, OK. Water has been chosen as the material of the detector because, like water, CR-39 PNTD has a tissue-like sensitivity to neutron. The dimension of the

detector, their placement inside the phantom, the shape of the phantom, and the treatment parameter mimic exactly the experimental design.

The same experimental configuration was used, except the phantom, for the study of neutrons in air. The schematic diagram of detectors location in air is shown in Figure 4.4.

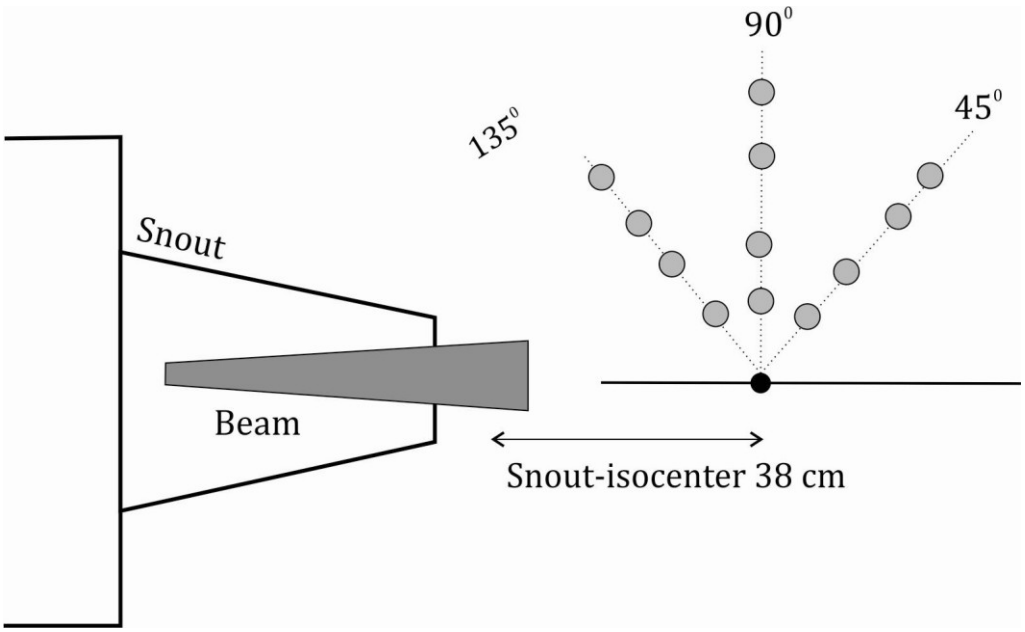

Figure 4.4: Diagram of the experimental setup in air. Circles represent the detectors locations.

The study with the presence and absence of phantom will allow us to understand the neutron sources and their respective contributions to the total absorbed dose and dose equivalent.

4.4 *Beam Interaction with snout and Phantom*

To reproduce the common treatment setup, an uncollimated beam of 18 x 18 cm^2 cross sectional area is created. The field size of the beam is produced by determining appropriate divergence of the beam such that a point source of protons will uniformly diverge to 20 x 20 cm^2 after travelling through 2 m in air. This beam is then allowed to pass through the simplified snout and the phantom used in this study. A FLUKA simulated 3D view of the interaction of the primary protons with snout and the phantom is shown in Figure 4.5. This plot demonstrates how the protons start from a point source far upstream and diverge on their way to the snout. The patient aperture in the snout shapes the beam to a 5 cm diameter before it hits the phantom. The interaction of the beam with snout creates the secondaries (blue lines) that scatter in all directions. This plot was created simulating a very low number of primary protons (10^3) for 162 MeV proton beam. The FLUKA simulations carried out to determine absorbed dose and dose equivalent consisted of a much larger number ($\sim 10^8$) primary protons.

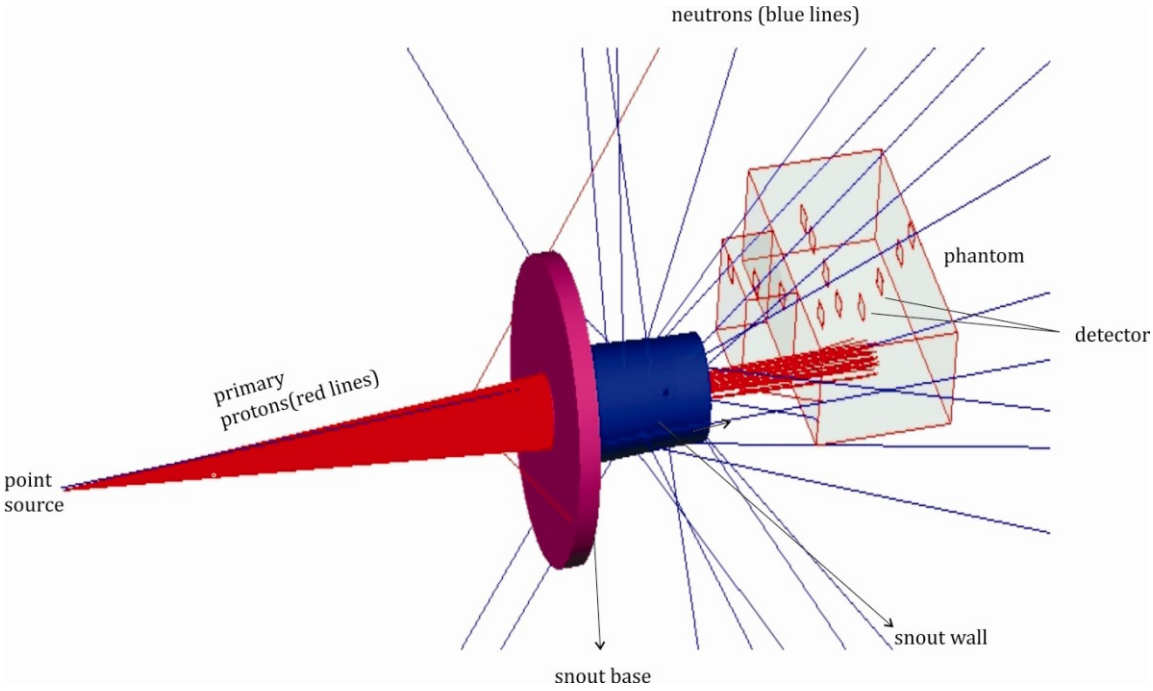

Figure 4.5: FLUKA simulated 3D view of a 162 MeV proton beam interacting with the snout and phantom.

A 2D view of the beam interaction with the snout and phantom is shown in Figure 4.6. This plot is also generated for a low number of primaries (10^3) in order to illustrate the primary beam path and the generation of secondary particles (mostly neutrons) by the primary proton beam. It can be seen from Figure 4.6 that the secondaries are scattered in all directions similar to what was seen in Figure 4.5.

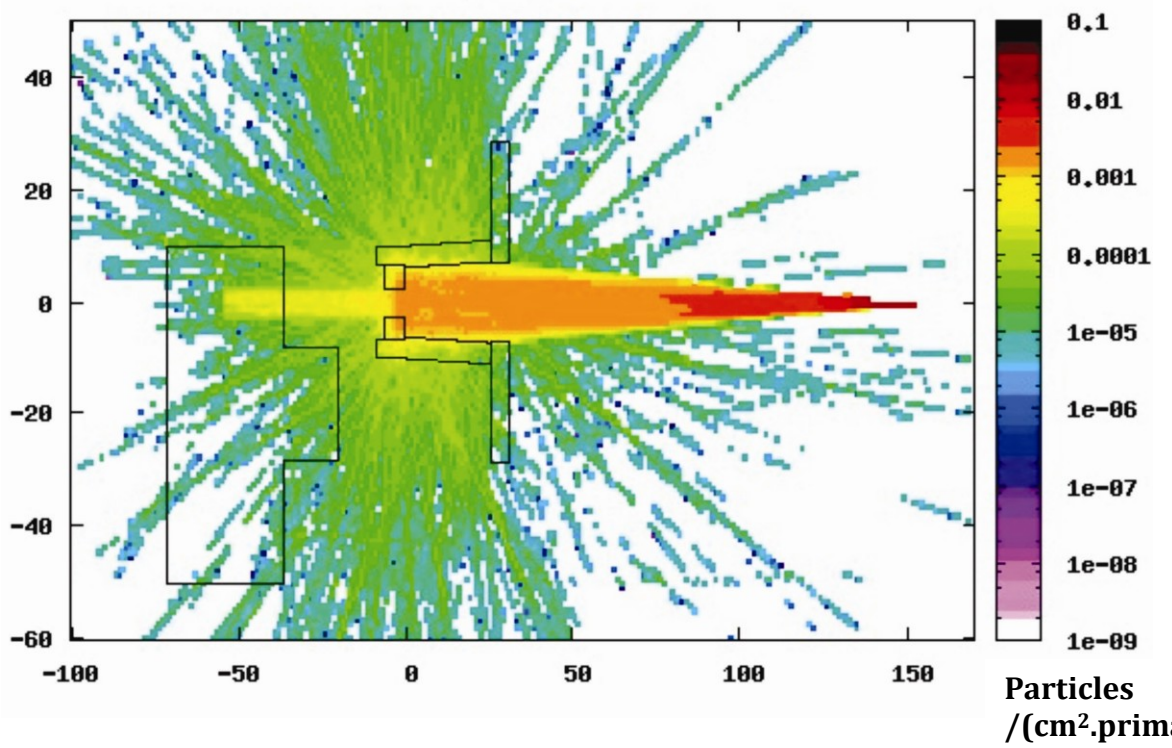

Figure 4.6: FLUKA simulated 2D view of 162 MeV primary beam interaction with snout and the phantom.

4.5 *SOBP Calculation*

For the calculation of SOBP, the effect of each layer of the range modulator needs to be simulated by running an individual primary beam of specific energy. A weighting factor, $w_{i,}$ is assigned for each layer and the dose for the SOBP was calculated by performing a weighted sum:

$$D/p = \sum_{i} w_i \, (D/p)_{i.} \qquad 4.1$$

The subscript, *i,* represents the number of the beam used in the process to produce the SOBP. The distal peak (highest energy) carries the highest weight and the proximal peak (lowest energy) carries lowest weight.

The dose equivalent is then found by:

$$\frac{H}{D} = \sum_{i} \frac{\left(\frac{H}{p}\right)}{\left(\frac{D}{p}\right)}. \qquad 4.2$$

The H term represents the dose equivalent per unit primary proton and the D term represents the respective dose per primary.

Appropriate weighting factors are important for the calculation of SOBP width as well as accurate dose deposition. A calculation of a 4 cm SOBP for 226 MeV proton beam is explained in this section. The first step was to determine the distal and proximal edge of the desired SOBP. For 226 MeV proton beam, the distal edge is 32 cm in water and to cover a 4 cm SOBP depth, the proximal edge needs to be at 28 cm, corresponding to a 208.5 MeV proton beam. Two more energies, 219 MeV and 213 MeV were used in between the distal and proximal edge for the overall uniformity of dose. Each beam was then run for the individual Bragg-peak. The dose at each Bragg-peak was then used to produce the SOBP by doing a weighted sum following Equation 4.1. The Bragg-peak of each individual beam and the weighted SOBP for 226 MeV protons is shown in Figure 4.7.

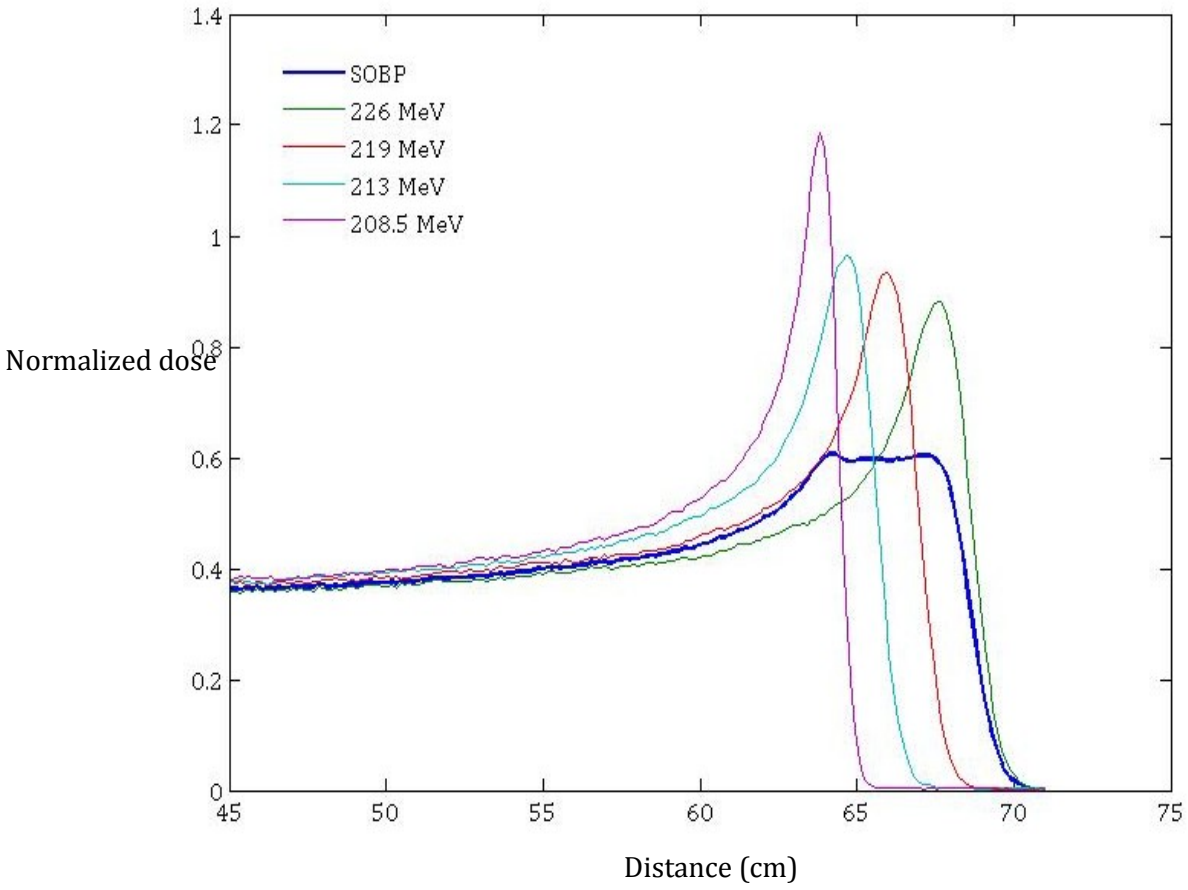

Figure 4.7: Bragg-peak of individual primary proton beam and the calculated SOBP for the maximum energy of 226 MeV.

The generated SOBP of 78 MeV, 162 MeV and 226 MeV proton beam is shown in Figure 4.8.

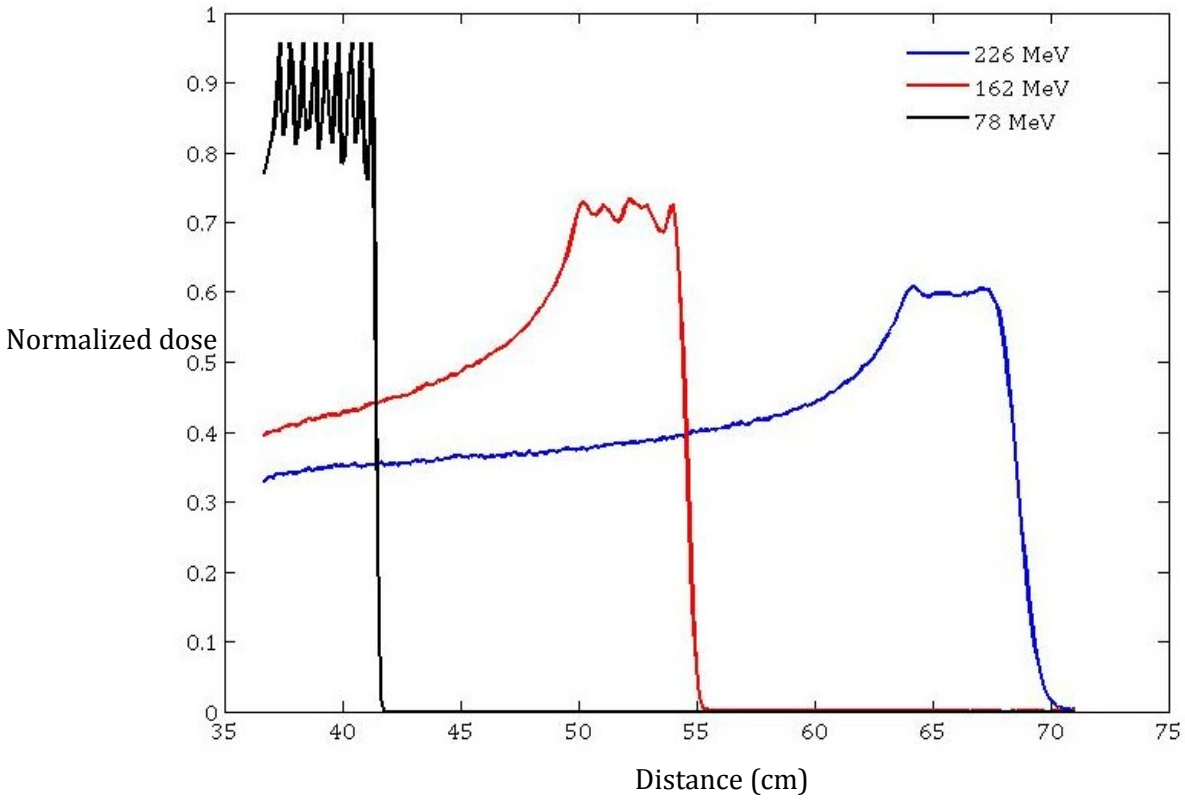

Figure 4.8: The generated SOBP for 78 MeV, 126 MeV and 226 MeV proton beam.

Figure 4.8 shows that the dose uniformity in the SOBP region is better for 226 MeV proton beams compared to 162 MeV and 78 MeV. This is because the width of Bragg-peak is inherently greater for 226 MeV protons than the other two beams, 162 MeV and 78 MeV, and this makes the SOBP region more uniform. The relatively larger width of the Bragg-peak for higher energy occurs due to the range strangling effect. In order to make a more uniform SOBP dose region for 162 MeV and 78 MeV protons, a large number of beams could be used. However, this is not practical in actual treatment situation.

CHAPTER 5

RESULTS

This chapter presents the off-axis dose equivalent from secondary neutrons at different locations in the presence and absence of a phantom as calculated by FLUKA. The dose equivalent is normalized to proton absorbed dose and is shown as the ratio of dose equivalent to absorbed proton dose (H_n/D_p). The dependence of off axis dose equivalent as functions of distance, energy, and angle is described. The fluence of secondary neutrons at different locations is also presented.

5.1 *Neutron dose equivalent inside the phantom and in air*

Table 5.1 lists the FLUKA calculated dose equivalent due to secondary neutrons at different locations inside the phantom and in air for a 78 MeV proton beam. In air, the detector locations were nearly identical to those inside the phantom, except at 90° where the detectors were placed at larger distances from isocenter (40 and 50 cm). The distance is measured off-axis to the primary beam from beam isocenter.

Table 5.1: FLUKA simulated ratios of neutron dose equivalent to proton absorbed dose (H_n/D_p) for a 78 MeV primary proton beam at detector locations inside the phantom and in air. All the distance is measured from beam isocenter.

Proton Beam (MeV)	Angle	Distance In phantom (cm)	H_n/D_p (mSv/Gy)	Distance in air (cm)	H_n/D_p (mSv/Gy)
			Phantom		Air
78	45°	7.5	1.51 ± 0.02	7.50	2.71 ± 0.12
		17.5	0.43 ± 0.01	16.3	2.11 ± 0.07
		28.5	0.21 ± 0.01	28.5	1.52 ± 0.08
		35.5	0.11 ± 0.01	35.0	1.21 ± 0.06
	90°	7.5	1.91 ± 0.02	12.5	3.41 ± 0.17
		17.5	0.52 ± 0.02	18.2	2.82 ± 0.12
		28.5	0.23 ± 0.01	40.0	2.23 ± 0.11
		35.5	0.13 ± 0.01	50.0	1.91 ± 0.07
	135°	7.5	3.81 ± 0.02	9.3	4.31 ± 0.21
		18.2	1.41 ± 0.02	17.2	5.03 ± 0.26
		25.5	1.02 ± 0.02	29.5	5.12 ± 0.27
		35.5	1.43 ± 0.01	33	4.71 ± 0.23

Figure 5.1 shows the neutron dose equivalent per proton absorbed dose (H_n/D_p) for 78 MeV proton beam inside the phantom. Inside the phantom, H_n/D_p ranged from 0.11 ± 0.01 to 3.81 ± 0.02 mSv/Gy, and in air it ranged from 1.21 ± 0.06 to 5.12 ± 0.27 mSv/Gy for 78 MeV proton beam. In general, H_n/D_p decreases with distance at all angles (45°, 90°, and 135°). The exception is increase of H_n/D_p observed at large distance (35.5 cm) at 135°. Most of the secondary neutrons are created by the patient aperture in the snout. At detector locations further away from the isocenter (see Figure 4.2 for detector locations), the neutron fluence decreases.

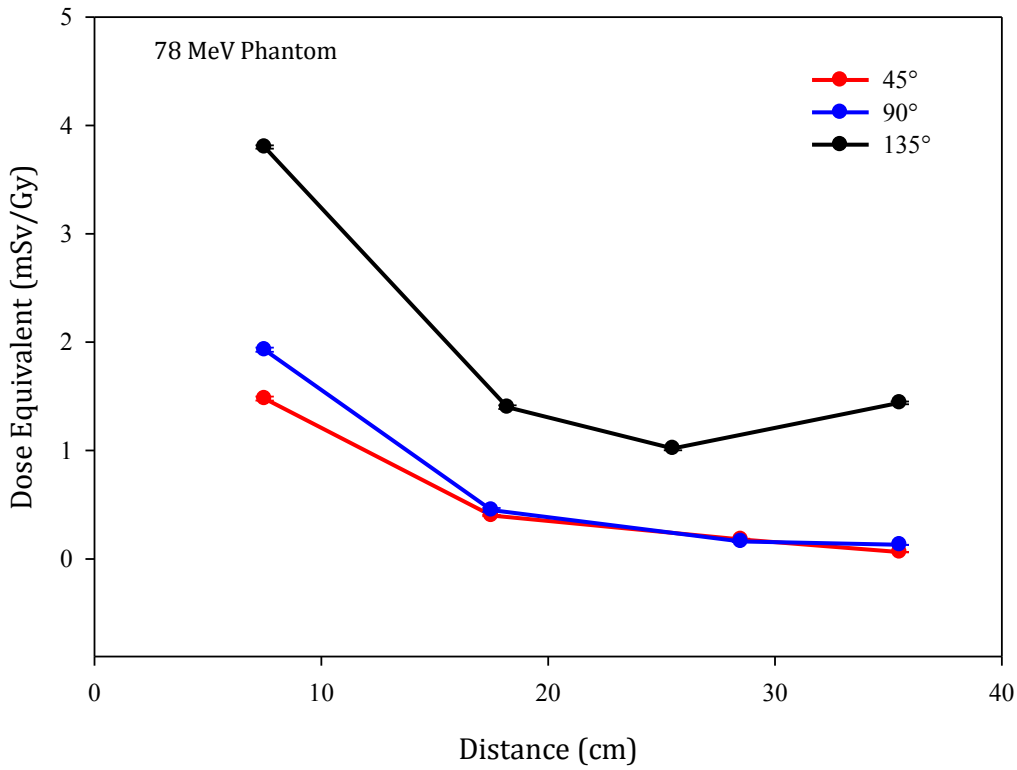

Figure 5.1: FLUKA simulated neutron dose equivalent per therapeutic proton absorbed dose, H_n/D_p, for a 78 MeV proton beam inside the phantom at increasing distances from isocenter at 45°, 90° and 135° to the direction of the beam.

The fluence spectrum for a 78 MeV proton beam inside the phantom at 90° for 7.5 cm, 17.5 cm, 28.5 cm, and 35.5 cm is shown Figure 5.2. The fluence spectrum is normalized by the total fluence at each location. The figure possesses two main peaks; the first peak is located at about 1 MeV and the second peak is located at about 30 MeV (barely visible). The peak at 1 MeV is due to low energy neutrons produced by evaporation process, while the peak near 30 MeV corresponds to high energy forward moving neutrons due to intranuclear cascades. The neutron fluence for energies ranging from 1 to 20 MeV (neutrons energy range used for scoring dose equivalent) shows that at 7.5 cm, the average fluence is higher compared to the

other distances (17.5 cm, 28.5 cm, 35.5 cm). At 90°, as the distance inside the phantom increases, neutrons need to travel a relatively longer path, which causes more neutron attenuation inside the phantom, resulting in a decrease in fluence. Since dose equivalent is related to the fluence, the decrease in neutron fluence results in a decrease of the H_n/D_p.

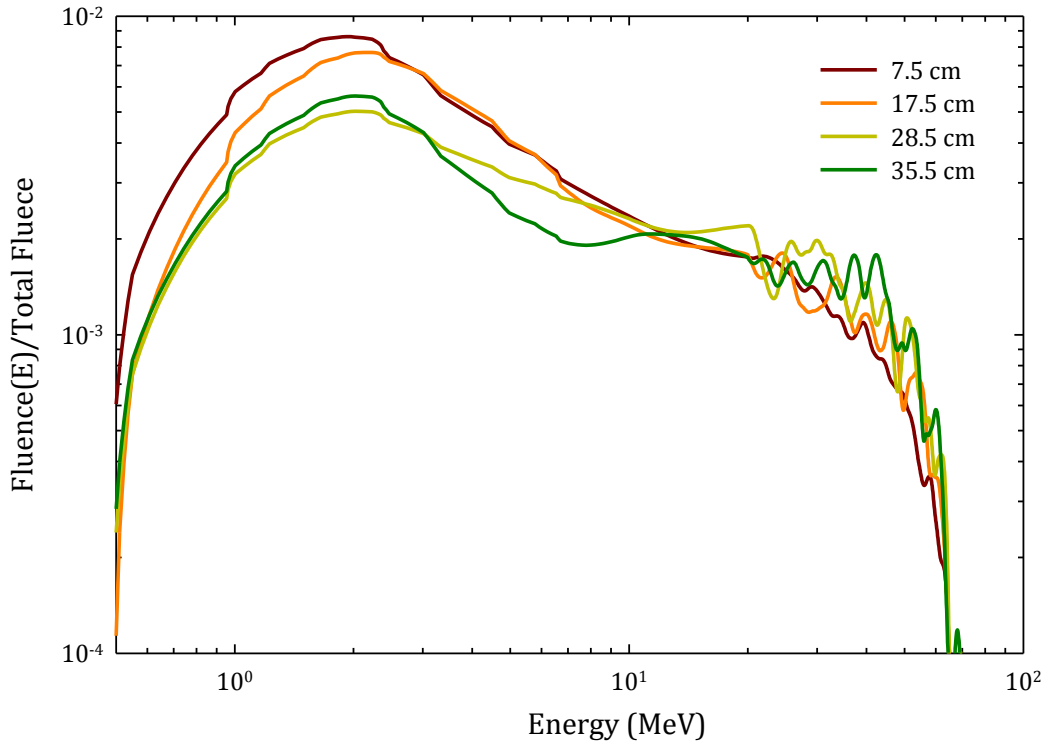

Figure 5.2: FLUKA simulated neutron spectrum from a 78 MeV proton beam inside phantom at 90° and 7.5 cm, 17.5 cm, 28.5 cm, and 35.5 cm from isocenter

The reason behind the increase in H_n/D_p at the larger distance (35.5 cm) at 135° inside the phantom is: a) at 135°, the detector was closer to the snout which caused a higher neutron fluence, and b) at 35.5 cm, the detector was closer to the front surface of the phantom, causing the neutrons not to be attenuated as much as they

would have at greater depths in the phantom. A similar trend of higher H_n/D_p near the front surface of the phantom was also observed at 135° compared to other angles by Shin et al. (Shin et al., 2009) for single and double scattering beam delivery systems.

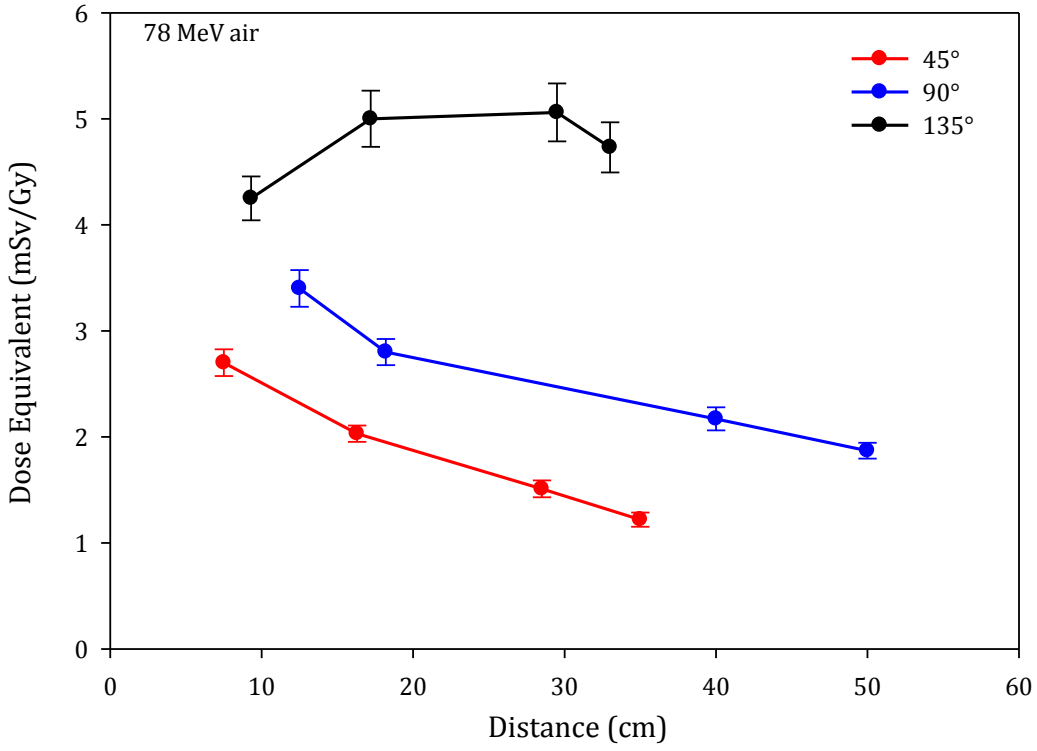

Figure 5.3: FLUKA simulated neutron dose equivalent per therapeutic proton absorbed dose, H_n/D_p, for a 78 MeV proton beam in air at increasing distances from isocenter at 45°, 90° and 135° to the direction of the beam.

Figure 5.3 shows the plot of H_n/D_p for a 78 MeV proton beam in air. A general decreasing trend in H_n/D_p with distance is again visible in air except at 135°, where H_n/D_p increases with distance. Overall, higher values of H_n/D_p can be seen in air versus inside the phantom at all angles as shown in Figure 5.4. This difference is due to the fact that more neutrons are stopped inside the phantom which is much

denser than air. This work is in agreement with the study carried by Zhang et. al. (Zhang et al., 2010).

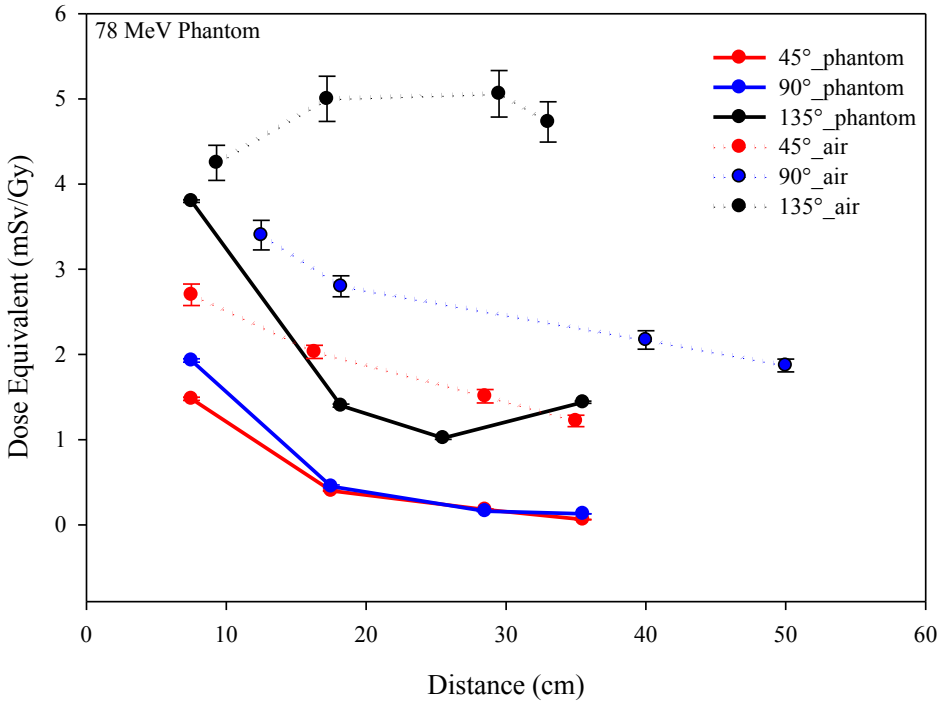

Figure 5.4: FLUKA simulated neutron dose equivalent per therapeutic proton absorbed dose, H_n/D_p, for a 78 MeV proton beams inside phantom and air at increasing distances from isocenter at 45°, 90° and 135° to the direction of the beam.

To help explain the increase in H_n/D_p in air with distances at 135°, secondary neutron fluence spectrum from 78 MeV at each location is calculated at 135° and is shown in Figure 5.5. This plot is shown for the energy range of 1 to 20 MeV. At smaller distance (9.3 cm), the fluence is lower while at larger distance (33 cm), the fluence is higher. This is because at larger distances from isocenter (33 cm), the neutron spectra contain more isotropic neutrons from evaporation processes than

forward moving neutrons. Due to these reasons, an increase in dose equivalent in air is observed at 135° as the distance increased from isocenter.

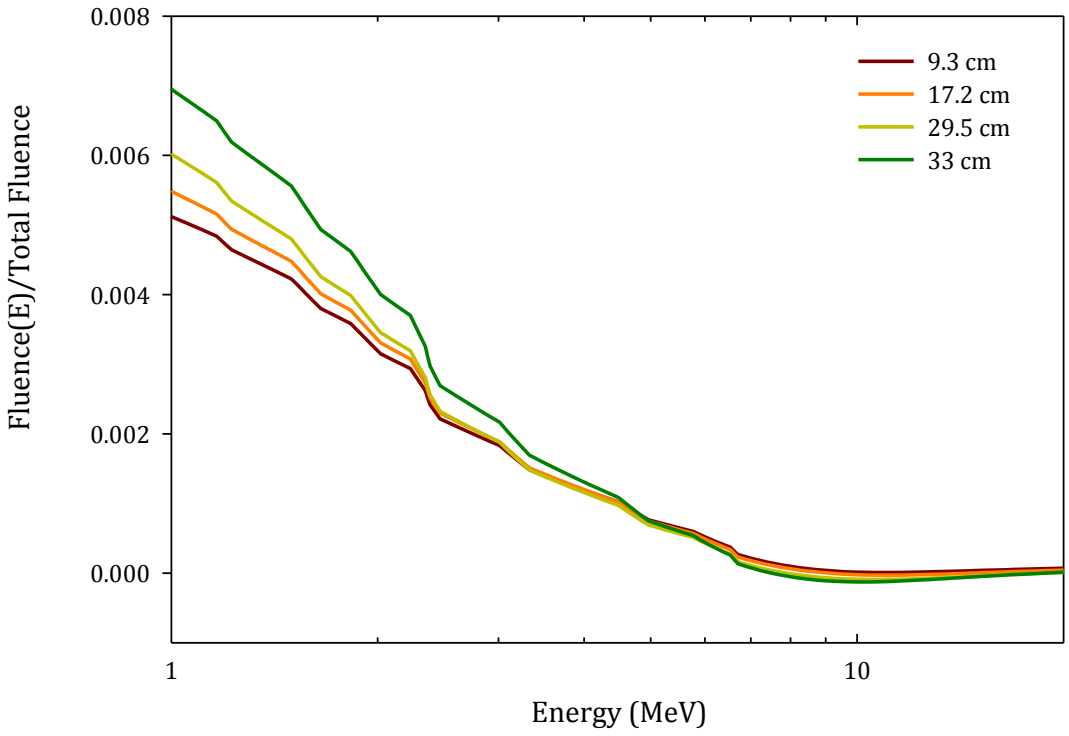

Figure 5.5. FLUKA simulated neutron spectrum for neutron energy of 1 to 20 MeV from a 78 MeV proton beam in air at 135° and 9.3 cm, 17.2 cm, 29.5 cm, and 33 cm from isocenter.

Table 5.2 lists the H_n/D_p value calculated by FLUKA for a 162 MeV proton beam inside the phantom and in air. Inside the phantom, H_n/D_p ranged from 1.01 ± 0.06 to 19.31 ± 0.24 mSv/Gy, and in air it ranged from 9.91 ± 0.34 to 39.31 ± 0.71 mSv/Gy.

Table 5.2: FLUKA simulated ratios of neutron dose equivalent to proton absorbed dose (H_n/D_p) for a 162 MeV primary proton beam at detector locations inside the phantom and in air. All the distance is measured from beam isocenter.

Proton Beam (MeV)	Angle	Distance in phantom (cm)	H_n/D_p (mSv/Gy) Phantom	Distance in Air (cm)	H_n/D_p (mSv/Gy) Air
162	45°	7.5	14.12 ± 0.67	7.5	21.51 ± 0.49
		17.5	5.41 ± 0.35	16.3	16.01 ± 0.38
		28.5	2.01 ± 0.21	28.5	11.72 ± 0.35
		35.5	1.01 ± 0.06	35	9.91 ± 0.34
	90°	7.5	16.61 ± 0.66	12.5	26.01 ± 0.52
		17.5	4.71 ± 0.24	18.5	21.02 ± 0.42
		28.5	2.12 ± 0.07	40	17.02 ± 0.47
		35.5	1.40 ± 0.07	50	14.01 ± 0.42
	135°	7.5	19.31 ± 0.24	7.5	33.21 ± 0.53
		18.2	13.32 ± 0.65	16.3	39.31 ± 0.71
		25.5	10.21 ± 0.20	28.5	39.22 ± 0.78
		33	12.51 ± 0.21	35	36.52 ± 0.73

Figure 5.6, Figure 5.7, and Figure 5.8 shows the H_n/D_p as a function of distance from isocenter for a 162 MeV proton beam inside the phantom, in air, and in phantom versus in air, respectively. The H_n/D_p trend for the 162 MeV proton beam is similar to that observed for the 78 MeV proton beam both in the presence of phantom and in the absence of a phantom, i.e. air. Also similar to the 78 MeV proton beam, H_n/D_p is seen to increase inside the phantom at largest distance (35.5 cm) at 135°, and in air the increase of H_n/D_p is observed at 135° at nearly all distances.

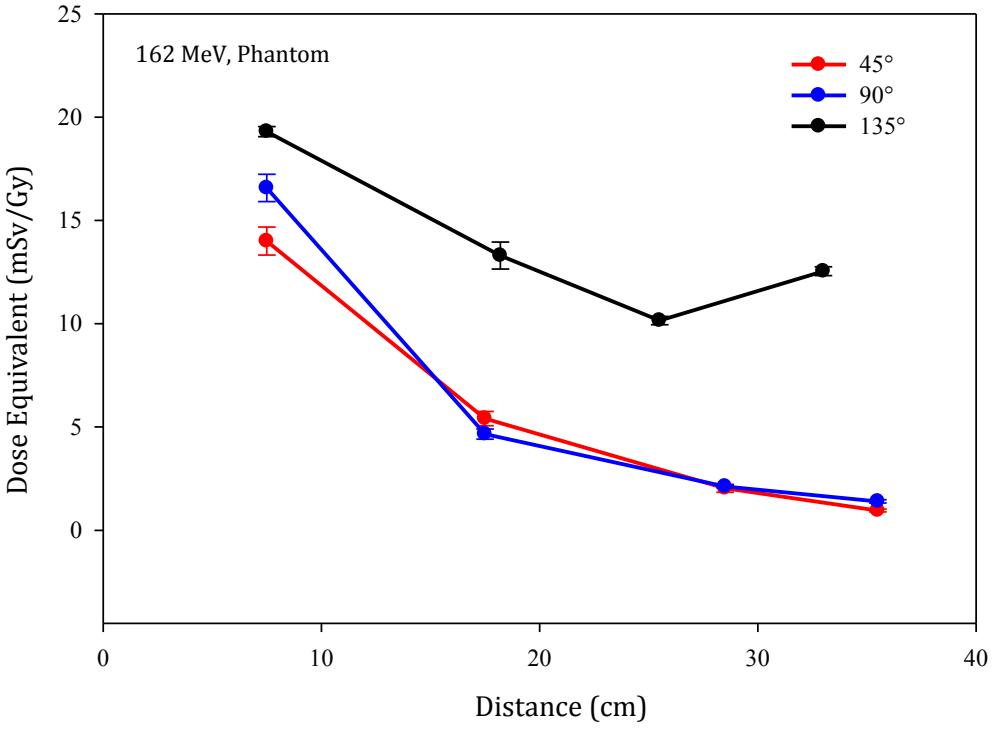

Figure 5.6: FLUKA simulated neutron dose equivalent per therapeutic proton absorbed dose, H_n/D_p, for a 162 MeV proton beam inside a phantom at increasing distances from isocenter at 45°, 90° and 135° to the direction of the beam.

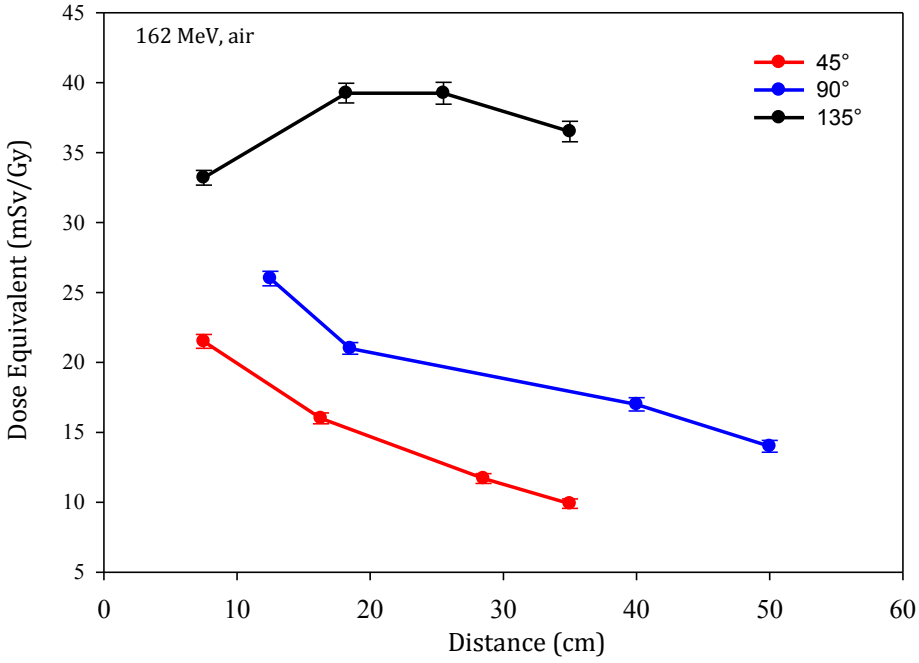

Figure 5.7: FLUKA simulated neutron dose equivalent per therapeutic proton absorbed dose, H_n/D_p, for a 162 MeV proton beam in air at increasing distances from isocenter at 45°, 90° and 135° to the direction of the beam.

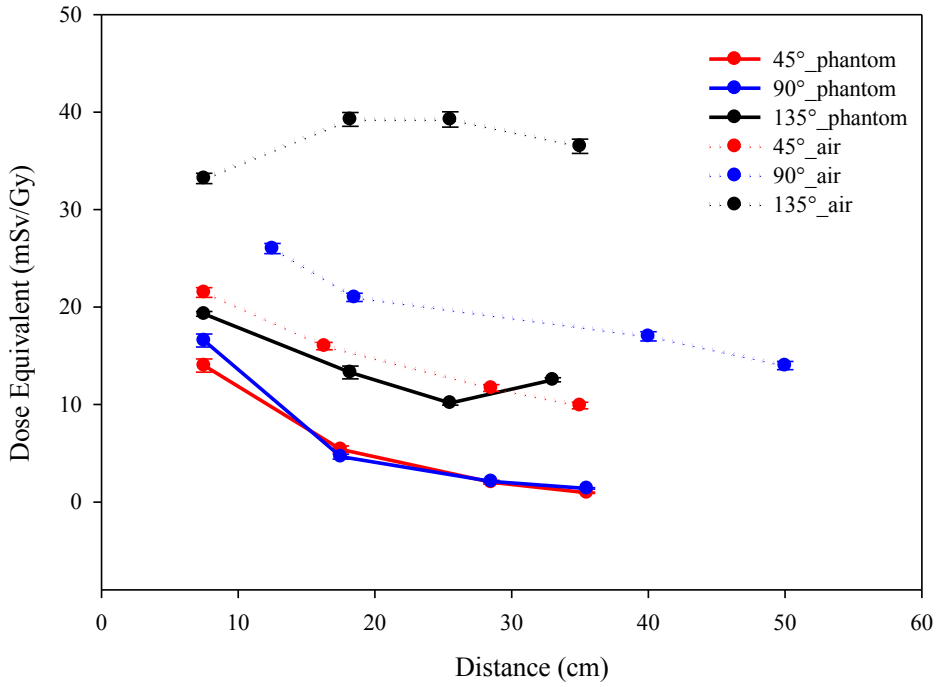

Figure 5.8: FLUKA simulated neutron dose equivalent per therapeutic proton absorbed dose, H_n/D_p, for a 162 MeV proton beams inside phantom and in air at increasing distances from isocenter at 45°, 90° and 135° to the direction of the beam.

Table 5.3 lists the H_n/D_p values calculated by FLUKA for a 226 MeV proton beam inside a phantom and in air. Inside the phantom, H_n/D_p ranged from 2.51 ± 0.14 to 69.21 ± 1.11 mSv/Gy, and in air it ranged from 24.81 ± 0.82 to 111.01 ± 1.99 mSv/Gy. Figure 5.9, Figure 5.10, and Figure 5.11 shows H_n/D_p as a function of distance from isocenter for 226 MeV proton beam inside the phantom, in air, and in the phantom versus in air, respectively. Again, the H_n/D_p trend for 226 MeV is similar to those observed for 78 MeV and 162 MeV proton beams both in the presence of a phantom and in air. In addition, an increase in H_n/D_p was seen at 135° in air and at larger (25.5 and 35.5 cm) distances in the phantom.

Table 5.3: FLUKA simulated ratios of neutron dose equivalent to proton absorbed dose (H_n/D_p) for a 226 MeV primary proton beam at detector locations inside the phantom and in air. All the distance is measured from beam isocenter.

Proton Beam (MeV)	Angle (degree)	Distance in phantom (cm)	H_n/D_p (mSv/Gy) Phantom	Distance in Air (cm)	H_n/D_p (mSv/Gy) Air
226	45°	7.5	28.61 ± 0.86	7.5	54.01 ± 1.25
		17.5	12.11 ± 0.61	16.3	40.31 ± 1.08
		28.5	5.01 ± 0.25	28.5	30.11 ± 0.91
		35.5	2.51 ± 0.14	35	24.81 ± 0.82
	90°	7.5	35.41 ± 0.92	12.5	66.11 ± 1.32
		17.5	11.51 ± 0.52	18.2	57.41 ± 1.32
		28.5	5.52 ± 0.25	40	45.02 ± 1.26
		35.5	4.01 ± 0.19	50	38.31 ± 1.14
	135°	7.5	69.21 ± 1.11	9.3	85.31 ± 1.80
		18.2	33.12 ± 0.86	17.2	106.71 ± 1.92
		25.5	38.03 ± 0.82	29.5	111.01 ± 1.99
		33	58.04 ± 0.99	33	101.01 ± 2.32

However, in contrast to the 78 MeV and 162 MeV proton beams, the 226 MeV proton beam at 135° shows an increase in H_n/D_p at a distance of 25.5 cm from isocenter as well as at 35.5 cm (Figure 5.9). This is because in a 226 MeV proton beam, the average energy of the neutrons is greater than the average energy of the neutrons created in both 78 MeV and 162 MeV proton beams. Due to this increase in average energy, the neutrons are less attenuated in the front region of the phantom. In other words, when neutron energy is larger, the cross section (interaction probability) of the neutrons with the phantom decreases. As a result at 135°, H_n/D_p for higher energy, neutrons in the phantom start to behave similar to H_n/D_p in air.

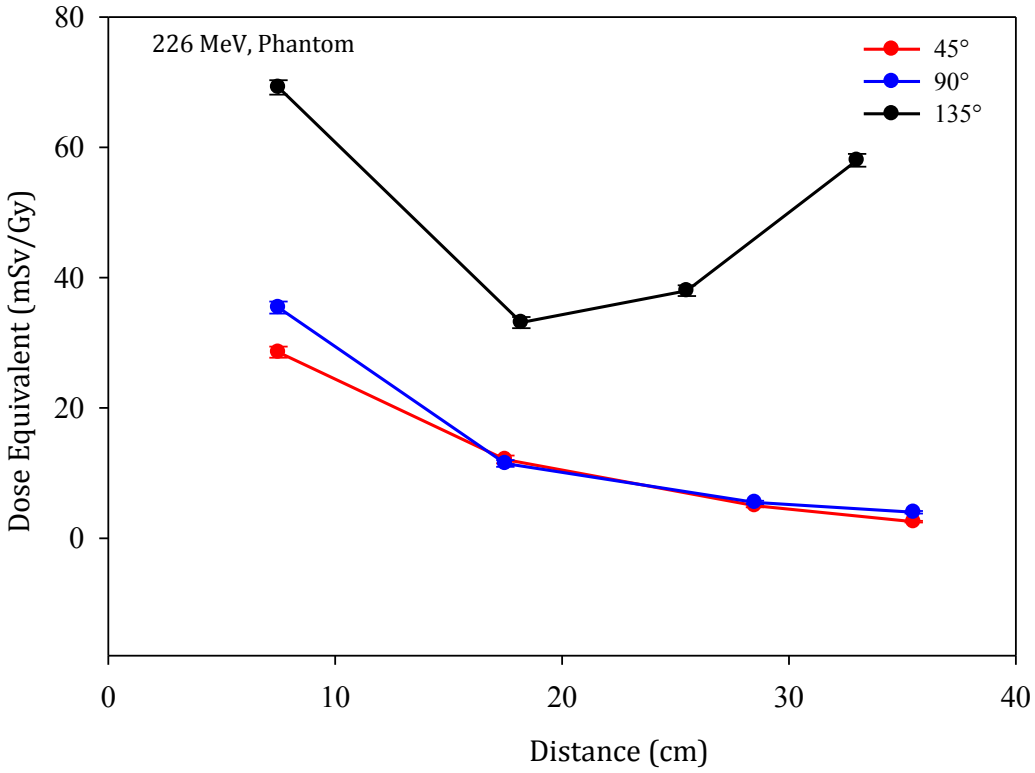

Figure 5.9: FLUKA simulated neutron dose equivalent per therapeutic proton absorbed dose, H_n/D_p, for a 226 MeV proton beam inside a phantom at increasing distances from isocenter at 45°, 90° and 135° to the direction of the beam.

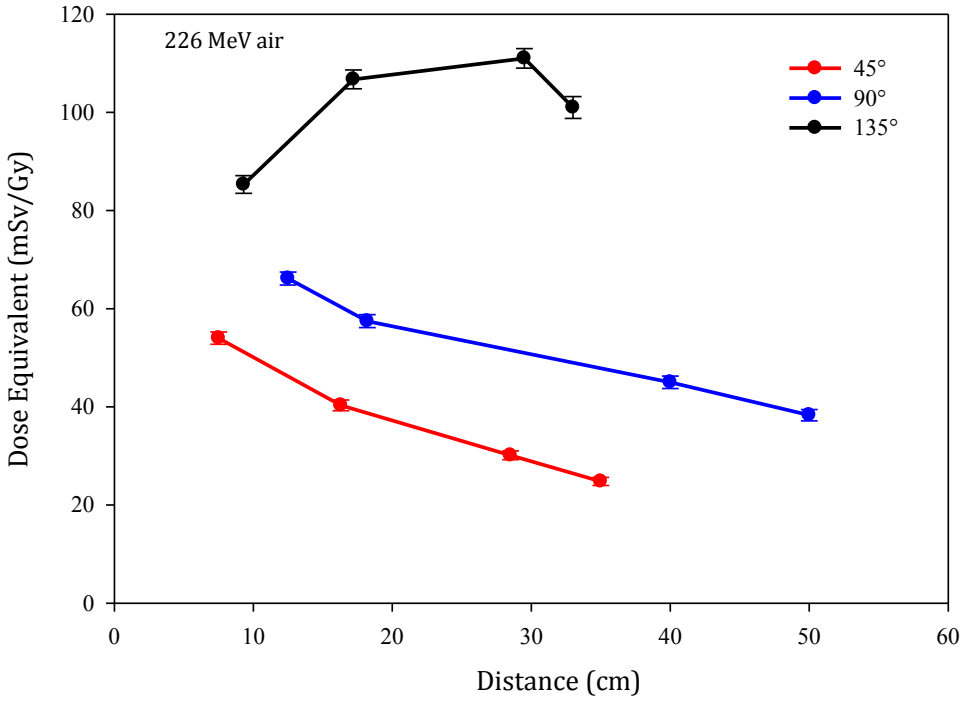

Figure 5.10: FLUKA simulated neutron dose equivalent per therapeutic proton absorbed dose, H_n/D_p, for a 226 MeV proton beam in air at increasing distances from isocenter at 45°, 90° and 135° to the direction of the beam.

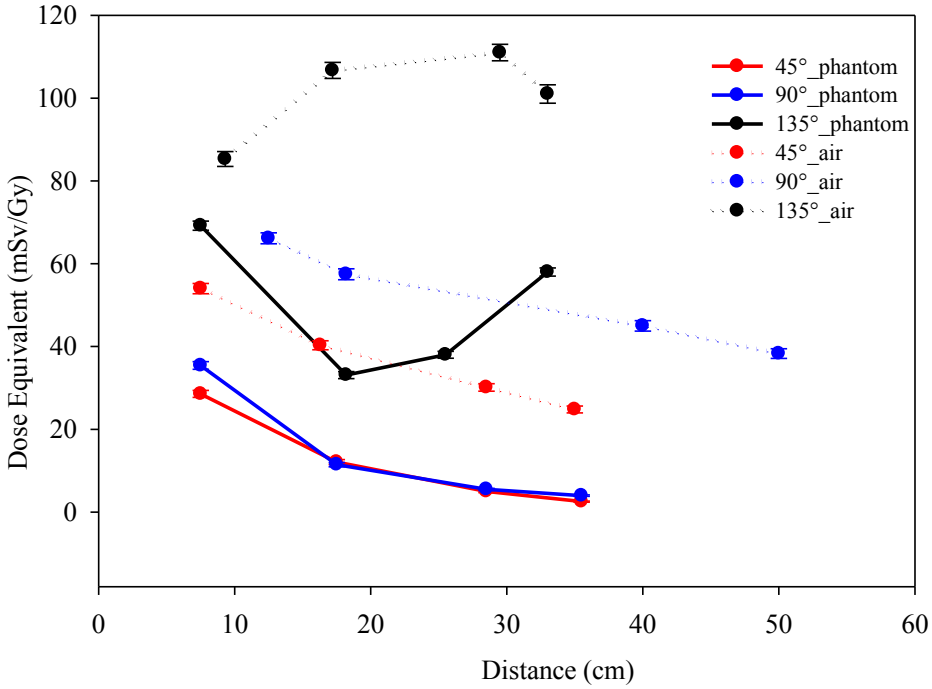

Figure 5.11: FLUKA simulated neutron dose equivalent per therapeutic proton absorbed dose, H_n/D_p, for a 226 MeV proton beam inside a phantom and in air at increasing distances from isocenter at 45°, 90° and 135° to the direction of the beam.

5.2 *Neutron dose equivalent dependence on energy*

To observe the dependence of H_n/D_p with energy, the detector at 17.5 cm from isocenter for all three angles is chosen. The schematic representation is shown in Figure 5.12. Figure 5.13 shows H_n/D_p as a function of proton energy at 17.5 cm from the beam isocenter and at 45°, 90°, and 135° inside the phantom and in air.

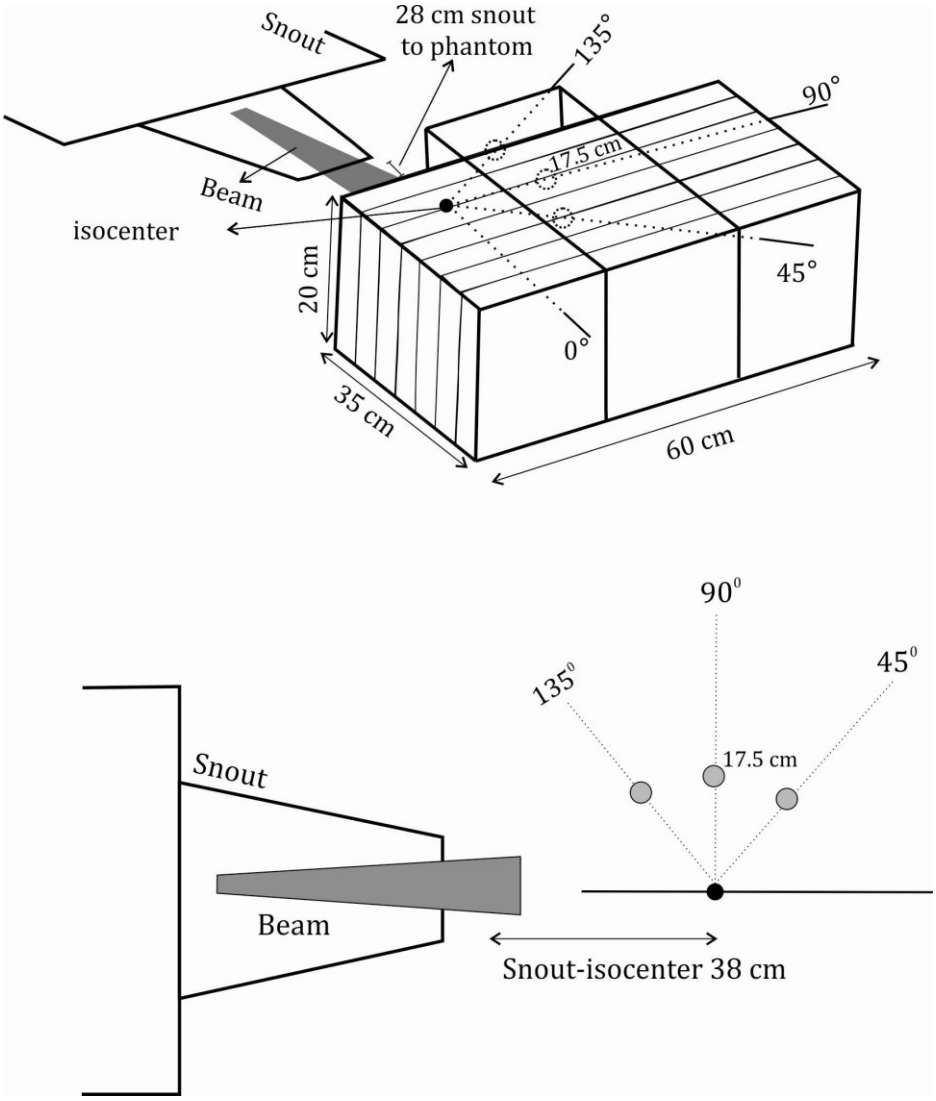

Figure 5.12: Diagram of the locations where dose equivalent was calculated at 17.5 cm from isocenter inside the phantom (top) and in air (bottom).

The general trend of H_n/D_p demonstrates that the energy of the primary beam increases the absorbed dose due to neutrons increases. The highest dose is observed for 226 MeV protons and the dose progressively goes down for 162 MeV and 78 MeV protons, respectively. For example, at 17.5 cm inside the phantom and at 90° to the primary beam, the H_n/D_p decreases from 11.51 ± 0.52 mSv/Gy for 226 MeV protons to 0.52 ± 0.02 mSv/Gy for 78 MeV protons, while in air the H_n/D_p decreases from 57.41 ± 1.32 mSv/Gy for 226 MeV protons to 2.82 ± 0.12 mSv/Gy for 78 MeV protons. This is expected since higher energy protons create more neutrons when they undergo nuclear interactions in the nozzle. The effective scan area is also an important parameter in neutron production for uniform scanning beam systems, since a larger effective area results in greater neutron production.

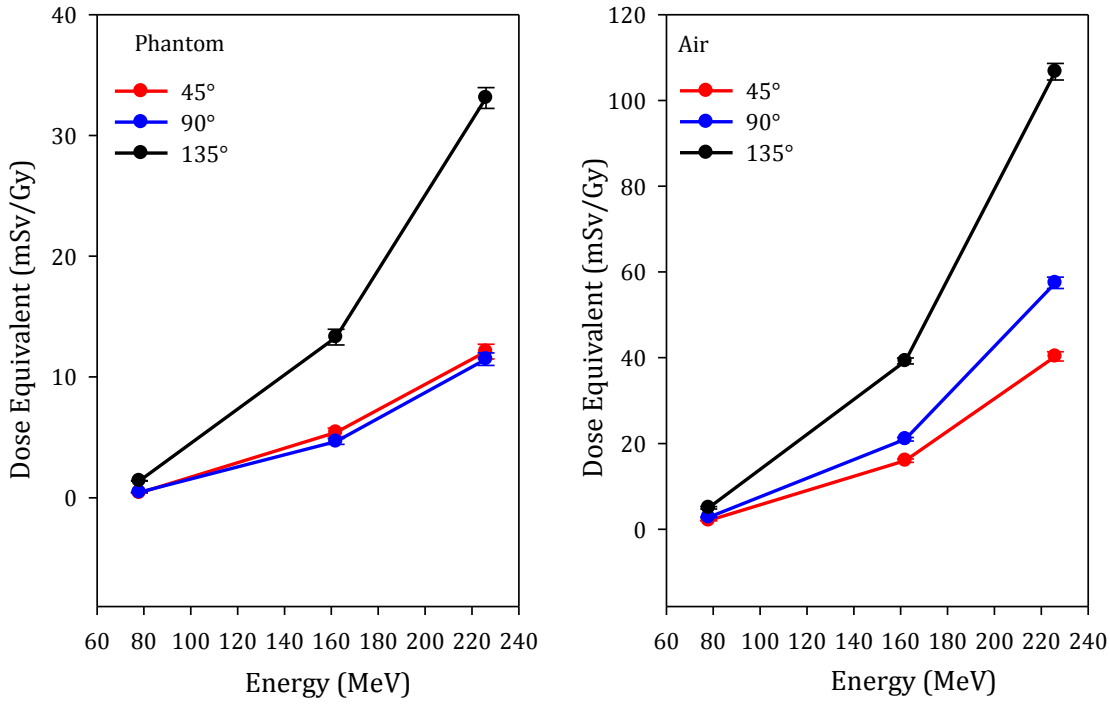

Figure 5.13: FLUKA simulated neutron dose equivalent per therapeutic proton absorbed dose, H_n/D_p, at 17.5 cm, 90° to primary beam, for 78 MeV, 162 MeV and 226 MeV protons inside a phantom (left) and in air (right).

5.3 *Dependence of* dose *equivalent on angle*

H_n/D_p as a function of measured angle with respect to the beam for a fixed distance of 17.5 cm for all three proton energies inside the phantom and in air is shown in Figure 5.14. As the angle increases from 45° to 135°, H_n/D_p inside the phantom increases by up to a factor of 3.5 at 17.5 cm for 78 MeV protons, 2.4 for 162 MeV protons and 2.7 for 226 MeV protons. The general trend of dose increase was also observed for each energy, though at 90° a decrease in dose equivalent was also observed in phantom as the angle increased. It could be that in phantom in the 45° detectors the forward moving neutrons (>~10 MeV) make a significant contribution in addition to isotropic neutrons (<10 MeV), but that at 90° the contribution from forward moving neutrons becomes less, leading to the decrease seen in H_n/D_p. At 135°, the fluence from isotropic neutrons is higher as they are closer to the nozzle and this leads to an increase in H_n/D_p. However, in all cases both in phantom and in air, H_n/D_p at 135° is higher compared to H_n/D_p values measured at 45° and 90°.

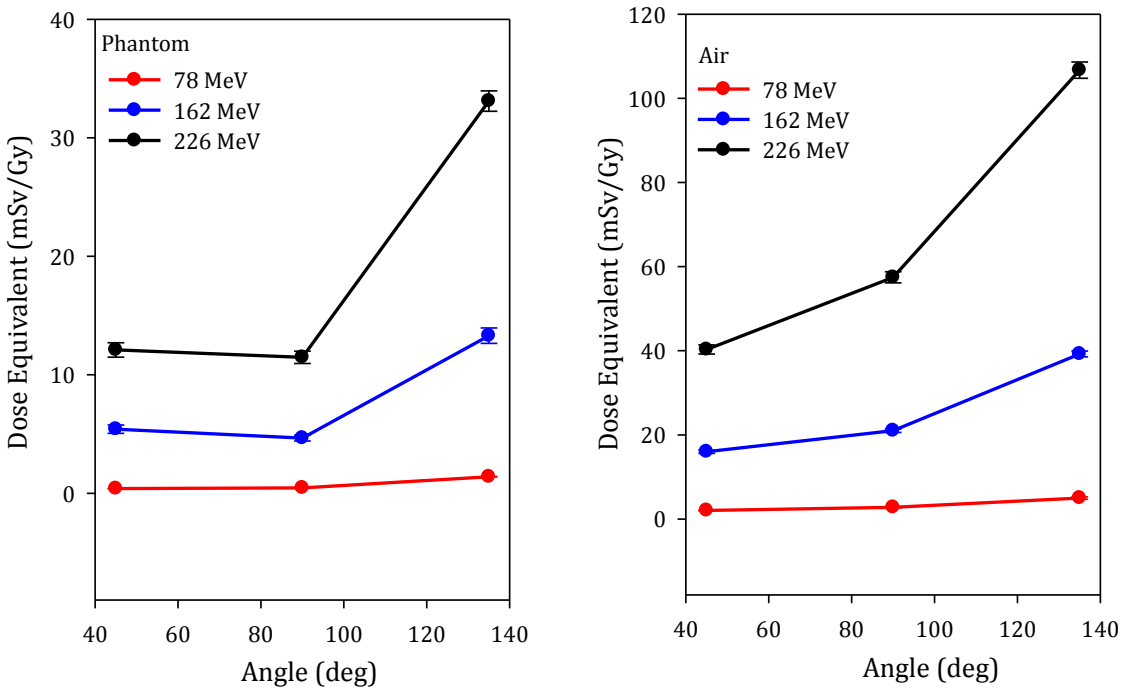

Figure 5.14: FLUKA simulated neutron dose equivalent per therapeutic proton absorbed dose, H_n/D_p, at 17.5 cm for 78 MeV, 162 MeV, 226 MeV protons inside the phantom (left), and in air (right).

CHAPTER 6

Discussion and Conclusions

The primary aim of this study was to determine the dose equivalent due to secondary neutrons for three different primary proton energies, 78 MeV, 162 MeV, and 226 MeV and a simplified snout configuration used in proton radiotherapy. We investigated the detailed spatial distribution of secondary neutron dose equivalent to primary proton dose, H_n/D_p, inside a phantom and in air for a fixed aperture size, fixed SOBP, and a fixed snout to surface distance using a uniform scanning nozzle at ProCure Proton Therapy Center, Oklahoma City, OK. This data can provide useful information for the radiation risk modeling from neutron exposure in proton radiotherapy.

In general, the ratio of dose equivalent from secondary neutrons calculated outside the treatment volume to primary proton dose, H_n/D_p, decreased with distance from beam isocenter both inside a phantom and in air. In air, H_n/D_p was observed to be higher than in the phantom for identical locations. Inside the phantom H_n/D_p ranged from 0.11 ± 0.01 to 3.81 ± 0.02 mSv/Gy for a 78 MeV proton beam, 1.01 ± 0.06 to 19.31 ± 0.24 mSv/Gy for a 162 MeV proton beam, and 2.51 ± 0.14 to

69.21 ± 1.11 mSv/Gy for a 226 MeV proton beam, respectively. In air H_n/D_p values ranged from 1.21 ± 0.06 to 4.31 ± 0.21 mSv/Gy for a 78 MeV proton beam, 9.91 ± 0.34 to 39.31 ± 0.71 mSv/Gy for a 162 MeV proton beam, and 24.81 ± 0.82 to 111.01 ± 1.99 mSv/Gy for a 226 MeV proton beam, respectively.

Comparison of data from this study with the results from other beam line designs and patient specific factors is difficult since the treatment nozzle and beam condition vary from facility to facility and neutron dose equivalent varies greatly between different beam delivery systems. However, relative comparisons of similar setups can be made. A comparison of results for 78 MeV and 162 MeV proton beams from this study with different uniform scanning and passive scattering studies is shown in Table 6.1. As shown in the table, results obtained in this study are consistent with previously published results (Zheng et al., 2012) for the same uniform scanning system. Zheng et al. reported that the H_n/D_p for 5 cm range proton beam, with a $30 \times 30 \times 30$ cm^3 phantom centered at isocenter, was 0.35 mSv/Gy for a 4 cm SOBP, where the detector location was 50 cm lateral to the primary axis. In the current study, H_n/D_p for the same beam conditions but 35.5 cm lateral to primary beam axis was 0.13 ± 0.01 mSv/Gy. Also shown in the table, Yan et al. (Yan et al., 2002) reported 4.5 mSv/Gy for 160 MeV protons at 50 cm, 8.2 cm modulation width, and with a phantom at isocenter of 26 cm diameter and 24 cm length. At that position in the current study for 162 MeV protons in air, H_n/D_p was 1.4 mSv/Gy. In a separate study, Polf and Newhauser (Polf and Newhauser, 2005) determined from Monte Carlo simulation H_n/D_p for similar experimental conditions

to those used by Yan et al. (Yan et al., 2002). They found H_n/D_p to be 3.9 mSv/Gy for a 160 MeV proton beam, 3 cm modulation width at 90^0 to the beam axis and 50 cm from the isocenter. This comparison indicates that the production of neutrons and corresponding values of H_n/D_p for the uniform scanning system is of a similar order of magnitude to that produced by a passive scattering system.

Table 6.1: Comparison of this study with other published work. The H_n/D_p value listed for 78 MeV proton beam of this study was measured at 35 cm from isocenter. The rest of the listed H_n/D_p values were measured at 50 cm from isocenter.

Type	Proton Beam (MeV)	H_n/D_p (mSv/Gy)
This study (uniform scanning)	78	0.1
Zheng et al (2012) (uniform scanning)	78	0.35
This study (uniform scanning)	162	1.4
Polf et.al (2005) (passive scattering)	160	3.9
Yan et al. (2002) (passive scattering)	160	4.5

The statistical uncertainty in the FLUKA simulation was around 5%, though the fluence to dose equivalent conversion in the simulation could add as much as 30% uncertainty to the values of H_n/D_p (Schneider et al., 2002). This study does not incorporate the contribution of H_n/D_p from thermal and epithermal neutrons (up to an energy of 1 MeV), because the detector we used in experiments was insensitive in that energy region. We are currently investigating the contributions from thermal and epithermal neutrons for uniform scanning beams. In addition, this study did not

include any range compensator which may lead to some differences with actual neutron dose equivalent to tissue surrounding the treatment volume in patient treatment. The whole study was conducted only for one particular setup of treatment parameters which might be different from an actual treatment scenario.

Currently, an experiment is in progress using the same setup that was used in these simulations. CR-39 PNTD is used in the experiments to measure the secondary neutron dose equivalent.

Also, in the future, a detailed simulation of beam delivery system for varying patient specific parameters, e.g. various beam scanning areas, different snout size, and different SOBP can be performed for the better estimation of H_n/D_p. This can help understanding the detail distribution of neutron dose in proton radiotherapy.

References

Aiginger H, Andersen V, Ballarini F, Battistoni G, Campanella M, Carboni M, Cerutti F, Empl A, Enghardt W, Fassò A, Ferrari A, Gadioli E, Garzelli M V, Lee K, Ottolenghi A, Parodi K, Pelliccioni M, Pinsky L, Ranft J, Roesler S, Sala P R, Scannicchio D, Smirnov G, Sommerer F, Wilson T and Zapp N 2005. The FLUKA code: New developments and application to 1 GeV/n iron beams. *Advances in Space Research,* **35,** 214-222.

Albertini F. 2011. *Planning and Optimizing Treatment Plans for Actively Scanned Proton Therapy: evaluating and estimating the effect of uncertainties.* PhD, Università degli Studi di Milano.

Andersen V, Ballarini F, Battistoni G, Campanella M, Carboni M, Cerutti F, Empl A, Fassò A, Ferrari A, Gadioli E, Garzelli M V, Lee K a O, Pelliccioni M, Pinsky L S, Ranft J, Roesler S, Sala P R and Wilson T L 2004. The FLUKA code for space applications: recent developments. *Advances in Space Research,* **34,** 1302-1310.

Arjomandy B, Sahoo N, Cox J, Lee A and Gillin M 2009. Comparison of surface doses from spot scanning and passively scattered proton therapy beams. *Phys. Med. Biol.,* **54,** N295-N302.

Ballarini F, Battistoni G, Brugger M, Campanella M, Carboni M, Cerutti F, Empl A, Fassò A, Ferrari A and Gadioli E 2007. The physics of the FLUKA code: Recent developments. *Advances in Space Research,* **40,** 1339-1349.

Battistoni G, Muraro S, Sala P R, Cerutti F, Ferrari A, Roesler S, Fassò A and Ranft J 2007. The FLUKA code: Description and benchmarking. *In:* ALBROW, M. & RAJA, R. (eds.) *Proceedings of the Hadronic Shower Simulation Workshop 2006.* Fermilab: AIP Conference Proceedings.

Benton E R. 2004. *Radiation Dosimetry At Aviation Altitude And In Low Earth Orbit.*

Bethe H 1930. Zur Theorie des Durchgangs schneller Korpuskularstrahlen durch Materie. *Annalen der Physik,* **5**.

Binns P J and Hough J H 1997. Secondary Dose exposures during 200MeV proton therapy *Radiat. Prot. Dos.,* **70,** 441-444.

Brenner D J, Elliston C D, Hall E J and Paganetti H 2009. Reduction of the secondary neutron dose in passively scattered proton radiotherapy, using an optimized pre-collimator/collimator. *Physics in Medicine and Biology,* **54,** 6065-6078.

Brenner D J and Hall E J 2008. Secondary neutrons in clinical proton radiotherapy: A charged issue. *Radiotherapy and Oncology,* **86,** 165-170.

Collums T L. 2012. *Comparison of plastics used in tissue equivalent proportional counters (TEPC) and development of a balloon borne TEPC* PhD, OKlahoma State University.

Das I J, Cheng C-W, Watts R J, Ahnesjö A, Gibbons J, Li X A, Lowenstein J, Mitra R K, Simon W E and Zhu T C 2008. Accelerator beam data commissioning equipment

and procedures: Report of the TG-106 of the Therapy Physics Committee of the AAPM. *Med. Phys.,* **35,** 4186-4214.
Decimal. 2013. *Decimal, The benchmark for custom radiation therapy* [Online]. Available: http://www.dotdecimal.com/products/protons [Accessed].
Delaney G, Jacob S, Featherstone C and Barton M 2005. The role of radiotherapy in cancer treatment: estimating optimal utilization from a review of evidence-based clinical guidelines. *Cancer,* **104,** 1129-37.
Dendale R, Lumbroso-Le R L, Noel G, Feuvret L, Levy C, Delacroix S, Meyer A, Nauraye C, Mazal A, Mammar H, Garcia P, D'hermies F, Frau E, Plancher C, Asselain B, Schlienger P, Mazeron J J and Desjardins L 2006. Proton beam radiotherapy for uveal melanoma: results of Curie Institut-Orsay proton therapy center (ICPO). *Int J Radiat Oncol Biol Phys,* **65**.
Devita V T, Oliverio V T and Muggia F M 1979. The drug development and clinical trials programs of the division of cancer treatment, National Cancer Institute. *Cancer Clin Trials,* **2,** 195-216.
DNA. 2013. *Explaning DNA* [Online]. Available: http://www.wellcome.ac.uk/en/fourplus/DNA.html [Accessed].
Dowdell S J. 2011. *Pencil Beam Scanning proton Therapy: The significance of secondary particles* PhD, University of Wollongong.
Farr J B, Mascia A E, Hsi W C, Allgower C E, Jesseph F, Schreuder A N, Wolanski M, Nichiporov D F and Anferov V 2008. Clinical characterization of a proton beam continuous uniform scanning system with dose layer stacking. *Med. Phys.,* **35,** 4945-4954.
Fassò A, Ferrari A, Ranft J and Sala P R 2005. FLUKA: a multi-particle transport code. CERN, INFN, SLAC.
Ferrari A, Pelliccioni M, Pillon M and Fluence to Effective Dose Equivalent Conversion Coefficients for Neutrons up to 10 Tev R P D, 165-173 (1997). 1997. Fluence to Effective Dose Equivalent Conversion Coefficients for Neutrons up to 10 TeV *Radiat. Prot. Dosim.,* **71,** 165-173.
Fluka. 2013. *A quick look at FLUKA's physics, structure and capabilities* [Online]. Available: http://www.fluka.org/fluka.php?id=man_onl&sub=3 [Accessed].
Goitein M 2008. *Radiation Oncology: A Physicist's-Eye View*, Spingerlink.
Gottschalk B 2004. Passive Beam Spreading in Proton Radiation Therapy.
Hall E and Giaccia A 2006. Radiology for the Radiologist. Sixth ed. Philadelphia: Lippincott Williams & Wilkins.
Hall E J 2006. Intensity-modulated radiation therapy, protons, and the risk of second cancers *Int. J. Radiat. Oncol. Biol. Phys. ,* **65,** 1-7.
Hecksel D, Anferov V, Fitzek M and Shahnazi K 2010. Influence of beam efficiency through the patient-specific collimator on secondary neutron dose equivalent in double scattering and uniform scanning modes of proton therapy. *Medical Physics,* **37,** 2910.
A Monte Carlo code for particle transport, 1994, Number 22, Los Alamos Science
Neutron Interactions: Part I, 2010, Presentation on Radiation Physics, Available: http://www.uthgsbsmedphys.org/gs02-0093/3.3a-howellneutronlecture01.pdf.
ICRP (International Commission on Radiological Protection) 1991 *ICRP Publication No. 60* (Oxford).

ICRP (International Commission on Radiological Protection), Conversion Coeffcients for use in Radiological Protection against External Radiation, ICRP Publication 74, Ann. ICRP 26, Pergamon Press (1996).
Fundamental Quantities and Units of Ionizing Radiation.
ICRU (International Commission on Radiological Units), 1998, Proton Dosimetry: Part 1. Beam Production, Beam Delivery and Measurement of Absorbed Dose, Report 59, (Bethasa MD).
ICRU (ntrenational Commision on Radiation Units and Measurements), 2007, Report 78, 7, Journal of the ICRU.
Jiang H, Wang B, Xu X G, Suit H D and Paganetti H 2005. Simulation of organ-specific patient effective dose due to secondary neutrons in proton radiation treatment. *Phys. Med. Biol.,* **50,** 4337-4353.
Joiner M and Kogel A V D 2009. *Basic Clinical Radiobiology,* London, Hodder Arnold.
Jones D T L and Schreuder A N 2001. Magnetically scanned proton therapy beams: rationales and principles. *Radiat Phys Chem,* **61,** 615-8.
Kanai T, Kawachi K, Kumamoto Y, Ogawa H, Yamada T, Matsuzawa H and Inada T 1980. Spot Scanning system for proton therapy. *Medical Physics,* **7,** 365-369.
Khan F 2003. *The physics of radiation therapy, 3rd edn.,* Baltimore, Williams & Wilkins.
Koehler A M, Schneider R J and Sisterson J M 1977. *Medical Physics,* **4,** 297-301.
Mesoloras G, Sandison G A, Stewart R D, Farr J B and Hsi W C 2006. Neutron scattered dose equivalent to a fetus from proton radiotherapy of the mother. *Medical Physics,* **33,** 2479-2489.
Moskvin V, Cheng C W, Zhao Q and Das I J 2012. Comment on comparison of secondary neutron dose. *Med. Phys.,* **39,** 2303-2305.
Moyers M F, Benton E R, Ghebremedhin A and Coutrakon G 2008. Leakage and scatter radiation from a double scattering based proton beamline. *Medical Physics,* **35,** 128.
NCI (National Cancer Institute), *Radiation Therapy for Cancer, 2013,* Available: http://www.cancer.gov/cancertopics/factsheet/Therapy/radiation.
NIST (National Institute of Standards and Technology), Stopping-power and range tables for protons, 2012, Available: http://physics.nist.gov/PhysRefData/Star/Text/PSTAR.html.
NNDC (National Nuclear Data Center), 2013, *Evaluated nuclear data file (ENDF)*, 2013, Available: http://www.nndc.bnl.gov/exfor/endf00.jsp.
Paganetti H 2007. The Impact of Protons on the Incidence of Second Malignancies in Radiotherapy. *Technology in Cancer Research and Treatment,* **6,** 661-662.
Patel R R and Arthur D W 2006. The emergence of advanced brachytherapy techniques for common malignancies. *Hematology/Oncology Clinics of North America,* **20,** 97-118.
Pe´Rez-Andu´Jar A, Delucajr. P M, Thornton A F, Fitzek M, Hecksel D and Farr J 2012. Microdosimteric Measurements for neutron-absorbed dose determination during proton therapy. *Radiation Protection Dosimetry,* **151,** 365-373.
Pelliccion M 1998. Radiation weighting factors and high energy radiation. *Radiation Protection Dosimetry,* **80,** 371-378.

Perez-Andujar A, Newhauser W D and Deluca P M 2009. Neutron Production from beam modifying devices in a modern double scattering proton therapy beam delivery system. *Phys. Med. Biol.,* **54,** 993-1008.
Polf J C, D N W and U T 2005. Patient neutron dose equivalent exposures outside of the proton therapy treatment field. *Radiation Protection Dosimetry,* **115,** 154-158.
Polf J C and Newhauser W D 2005. Calculations of neutron dose equivalent exposures from range-modulated proton therapy beams *Phys. Med. Biol.,* **50,** 3859-3873.
P Rinard, Neutron Interactions with Matter: Los Alamos Technical Report, Available: http://www.fas.org/sgp/othergov/doe/lanl/lib-www/la-pubs/00326407.pdf.
Roesler S and Stevenson G R 2006. deq99.f, A FLUKA user-routine converting fluence into effective dose and ambient dose equivalent, 2006, Safety Commission, Technical Note CERN SC-2006-070-RP-TN

Saha G B 2006. *Physics and Radiobiology of Nuclear Medicine* New York, Springer.
Schlegel W C, Bortfeld T and Grosu A L 2006. *New Technologies in Radiation Oncology,* Berlin, Heidelberg, New York, Springer Berlin.
Schneider U, Agosteo S, Pedroni E and Besserer J 2002. Secondary neutron dose during proton therapy using spot scaninng. *Int J Radiation Oncology Biol. Phys.,* **53,** 244-251.
Seltzer S M 1993. An assessment of the role of charged secondaries from nonelastic nuclear interactions by therapy proton beams in water. NISTIR 5221.
Shin D, Yoon M, Kwak J, Shin J, Lee S B, Park S Y, Kim D Y and Cho K H 2009. secondary neutron doses for several beam configuration for proton therapy.pdf. *Int J Radiat Oncol Biol Phys,* **74,** 260-265.
Sisterson J 2005. *Particle News Letter,* **36**.
Souhami R L and Tobias J S 1986. *Cancer and its management,* Oxford, Blackwell Scientific.
Steneker M, Lomax A and Schneider U 2006. ntensity modulated photon and proton therapy for the treatment of head and neck tumors. *Radiother Oncol. 2006 Aug;80(2):263-7. Epub 2006 Aug 17.,* **80**.
Sternheimer R M and Peierls R F 1971. General Expression for the Density Effect for the Ionization Loss of Charged Particles. *Physical Review B,* **3,** 3681-3692.
Tayama R, Fujita Y, Tadokor M, Fujimaki H, Sakae T and Terunuma T 2006. Measurement of neutron dose distribution for a passive scattering nozzle at the Proton Medical Research Center (PMRC). *Nuc. Inst. & Meth. A,* **564,** 532-536.
Terezakis S A, Heron D E, Lavigne R F, Diehn M and Billy W. Loo J 2011. What the Radiologist Needs to Know about Radiation Oncology. *Radiology,* **261,** 31-44.
Tobias J S 1996. The role of radiotherapy in the
management of cancer - an overview. *Ann Acad Med Singapore* **25,** 371-379.
Depth Dose Curves, Avaialbe: http://commons.wikimedia.org/wiki/File:Depth_Dose_Curves.jpg.
Yan X, Titt U and Koehler A 2002. Measurement of neutron dose equivalent to proton therapy patients outside of the proton radiation field *Nucl Instr Methods Phys Res,* **A476,** 429-434.

Zhang R, Pérez-Andújar A, Fontenot J D, Taddei P J and Newhauser W D 2010. An analytic model of neutron ambient dose equivalent and equivalent dose for proton radiotherapy. *Physics in Medicine and Biology,* **55,** 6975-6985.

Zheng Y, Fontenot J, Taddei P, Mirkovic D and Newhauser W 2008. Monte Carlo simulations of neutron spectral fluence, radiation weighting factor and ambient dose equivalent for a passively scattered proton therapy unit. *Physics in Medicine and Biology,* **53,** 187-201.

Zheng Y, Newhauser W, Fontenot J, Taddei P and Mohan R 2007a. Monte Carlo study of neutron dose equivalent during passive scattering proton therapy. *Physics in Medicine and Biology,* **52,** 4481-4496.

Zheng Y, Newhauser W and Mohan R 2007b. Monte Carlo study of neutron dose equivalent during passive scattering proton therapy. *Physics in Medicine and Biology,* **52,** 4481-4496.

Zheng Y, Yaxi L, Zeidan O, Schreuder A N and Keole S 2012. Measurements of neutron dose equivalent for a proton therapy center using uniform scanning proton beams. *Med. Phys.,* **39,** 3484-3492.

VITA

Mohammad Rafiqul Islam

Candidate for the Degree of

Master of Science

Thesis: OFF-AXIS NEUTRON STUDY FROM A UNIFORM SCANNING PROTON BEAM USING MONTE CARLO CODE FLUKA

Major Field: Physics

Biographical:

Education:

Completed the requirements for the Master of Science in Physics at Oklahoma State University, Stillwater, OK, in March 2013.

Completed the requirements for the Bachelor of Science in Physics at University of Dhaka, Bangladesh, in June 2003.